Wavelet transforms and their applications to MHD and plasma turbulence: a review

Marie Farge[1] and Kai Schneider[2],†

[1]LMD-CNRS, Ecole Normale Supérieure 24, Rue Lhomond, 75231 Paris CEDEX 6, France

[2]M2P2-CNRS, Aix-Marseille Université 38, Rue Frédéric Joliot-Curie, 13451 Marseille CEDEX 13, France

Wavelet analysis and compression tools are reviewed and different applications for the study of MHD and plasma turbulence are presented. We introduce the continuous and the orthogonal wavelet transform and detail several statistical diagnostics based on the wavelet coefficients. We then show how to extract coherent structures out of fully developed turbulent flows using wavelet-based denoising. Finally some multiscale numerical simulation schemes using wavelets are described. Several examples for analysing, compressing and computing one-, two- and three-dimensional turbulent MHD or plasma flows are presented.

---

1. Introduction

Turbulence is ubiquitous and plays a critical role for the plasma stability and confinement properties of fusion devices, e.g. in the tokamak edge region. Turbulence is a regime of fluid, gas and plasma flows characterized by highly nonlinear dynamics (Biskamp 1997). It exhibits a chaotic, i.e. unpredictible behaviour and rotational motion over a wide range of dynamically active scales. In contrast to classical dynamical systems, which are low dimensional and conservative, a turbulent flow is a dissipative dynamical system, whose behaviour is governed by a very large, possibly infinite, number of degrees of freedom. Each field, e.g. velocity, vorticity, magnetic field and current density, strongly fluctuates around a mean value and one observes that these fluctuations tend to self-organize into so-called coherent structures, i.e. vortex tubes in hydrodynamics and vorticity sheets and current sheets in magnetohydrodynamics (MHD). The presence of coherent structures results in strong spatial and temporal flow intermittency, which is a key feature of turbulence. Intermittency is understood here such that the fluctuations become stronger for decreasing scale and are hence more localized. The appropriate tool to study intermittency is the wavelet representation due to its intrinsic multiscale nature. Indeed, it yields a sparse multiscale representation of intermittent fields since wavelets are well localized functions in both physical and Fourier space.

The classical theory of homogeneous turbulence (Batchelor 1982) assumes that turbulent flows are statistically stationary and homogeneous. This allows the use of a Fourier space representation to analyse them (e.g. the energy spectrum is the

† Email address for correspondence: kschneid@cmi.univ-mrs.fr

modulus of the Fourier transform of the velocity auto-correlation), to model them (e.g. using large eddy simulation) and to compute them (e.g. using spectral methods). Hence, since the Fourier representation spreads information among the phases of all Fourier coefficients, the structural information (i.e. locality in time and in space) is lost when one considers only the modulus of the Fourier coefficients, as is usually done. This is a major drawback of the classical theory of turbulence and the reason why we proposed in Farge & Rabreau (1988) to replace the Fourier representation by the wavelet representation, to define new analyses and computational tools able to preserve information locally in time and space. If the Fourier representation is well suited to study linear dynamical systems (whose behaviour either persists at the initial scale or spreads over larger ones), this is not the case for nonlinear dynamical systems for which the superposition principle no more holds (i.e. they cannot be decomposed into a sum of independent subsystems to be separately studied). Moreover, the evolution of nonlinear dynamical systems develop over a wide range of scales, since energy is spread from the initially excited scale towards smaller and smaller scales (the so-called energy cascade) until finite-time singularities develop (e.g. shocks), unless some dissipative mechanisms damp energy and thus avoid its ultra-violet divergence. The art of predicting the evolution of nonlinear dynamical systems consists of disentangling their active components from their passive components, the former being deterministically computed while the latter are discarded or statistically modelled. One thus performs a distillation process to only retain the components essential to predict the nonlinear behaviour. The wavelet representation is particularly appropriate for this since it allows one to track the evolution in both space and scale and to only retain the degrees of freedom which determine the nonlinear dynamics. Turbulent flows are archetypes of nonlinear dynamical systems and therefore good candidates to be analysed, modelled and computed using the wavelet representation.

If we now focus on plasma turbulence, we are uneasy about the fact that we have two different descriptions, depending on which side of the Fourier transform we look from.

(i) We have a theory (Batchelor 1982) that assumes a nonlinear cascade in Fourier space for a range of scales, the so-called 'inertial range', where the flow kinetic energy is statistically (i.e. for ensemble of time or space averages) transferred towards smaller scales until reaching Kolmogorov's scale, where molecular dissipation transforms kinetic energy into heat. Under these hypotheses, the theory predicts a power-law behaviour for the modulus of the energy spectrum in the inertial range.

(ii) If we study the flow in physical space however, we do not have yet a predictive theory but only empirical observations (from laboratory and numerical experiments) showing the emergence and persistence of coherent structures, e.g. blobs and current sheets that concentrate most of the kinetic and magnetic energy, even for very high Reynolds number flows.

The classical methods for modelling turbulent flows, e.g. large eddy simulation (LES), suppose a scale separation (i.e. a spectral gap) and neglect the small-scale motions, although their effect on the large-scale motions is statistically modelled (supposing their dynamics to be linear or slaved to them). Unfortunately, for those methods we have strong evidence, from both laboratory and numerical experiments, that there is no spectral gap since all scales of the inertial range are coupled and interact nonlinearly. Moreover, one observes that coherent structures play a major dynamical role and are responsible for the transport and mixing properties

of turbulent flows. As a consequence, one might ask the following questions: are coherent structures the dynamical building blocks of turbulent flows and can we extract them? If we succeed to do so, would it be possible to represent them with a reduced number of degrees of freedom and would those be sufficient to compute the flow nonlinear dynamics?

The aim of this review is to offer a primer on wavelets for both continuous and orthogonal transforms. We then detail different diagnostics based on wavelet coefficients to analyse and to compress turbulent flows by extracting coherent structures. Examples for experimental data come from the tokamak Tore Supra (Cadarache, France) and numerical simulation data of resistive drift-wave and MHD turbulence illustrate the wavelet tools. Wavelet-based density estimation (WBDE) techniques to improve particle-in-cell (PIC) numerical schemes are presented, together with a particle-in-wavelet (PIW) scheme that we developed for solving the Vlasov–Poisson equations directly in wavelet space. Coherent vorticity and current sheet simulation (CVCS), that applies wavelet filtering to the resistive non-ideal MHD equations, is proposed as a new model for turbulent MHD flows. It allows one to reduce the number of degrees of freedom necessary to compute them, while capturing the nonlinear dynamics of the flow. This review is based on the work and publications we have performed within the last 15 years, in collaboration with the CEA-Cadarache and other teams in France, Japan and the United States. Almost all material presented here has already been published in our papers (cited in the references), and parts have been adapted for this review. Let us only mention a few references of wavelet techniques that have been used to analyse and quantify plasma turbulence: e.g. transients (Dose, Venus & Zohm 1997), bicoherence (Dudok De Wit & KrasnoselSkikh 1995; Van Milligen *et al.* 1995*a*; Van Milligen, Hidalgo & Sanchez 1995*b*; Dudok De Wit *et al.* 2014), intermittency (Carbone *et al.* 2000) and anisotropy (Alexandrova, Lacombe & Mangeney 2008). An exhaustive review is beyond the scope of our paper and we focus here exclusively on our contributions.

The outline of this review is the following: first, in § 2 we present wavelet analysis tools, including a short primer on continuous and orthogonal wavelets. Statistical tools in wavelet coefficient space are also introduced. Section 3 focuses on coherent structure extraction using wavelet-based denoising. Wavelet-based simulation schemes are reviewed in §§ 4 and 5 draws our conclusions.

2. Wavelet analysis

2.1. *Wavelets: a short primer*

2.1.1. *Continuous wavelet transform*

The wavelet transform (Grossmann & Morlet 1984) unfolds any signal (e.g. in time) or any field (e.g. in three-dimensional space) into both space (or time) and scale (or time scale), and possibly directions (for dimensions higher than one). The building block of the wavelet transform is the 'mother wavelet', $\psi(x) \in L^2(\mathbb{R})$ with $x \in \mathbb{R}$, that is a well-localized function with fast decay at infinity and at least one vanishing moment (i.e. zero mean). It is also smooth enough in order that its Fourier transform, $\hat{\psi}(k)$, exhibits fast decay for $|k|$ tending to infinity. From the mother wavelet one then generates a family of wavelets, translated by $b \in \mathbb{R}$, the position parameter, dilated (or contracted) by $a \in \mathbb{R}^+$, the scale parameter, and normalized in L^2-norm (i.e. $\|\psi_{a,b}\|_2 = 1$) to obtain the set

$$\psi_{a,b}(x) = \frac{1}{\sqrt{a}} \psi\left(\frac{x-b}{a}\right). \tag{2.1}$$

The wavelet transform of $f \in L^2(\mathbb{R})$ is the inner product of f with the analysing wavelets $\psi_{a,b}$, and the wavelet coefficients that measure the fluctuations of f at scale a and position b given by

$$\widetilde{f}(a, b) = \langle f, \psi_{a,b} \rangle = \int_{\mathbb{R}} f(x) \psi_{a,b}^{\star}(x) \, \mathrm{d}x, \qquad (2.2)$$

with $\star$ denoting the complex conjugate. The function f is reconstructed from its wavelet coefficients, as the inner product of $\widetilde{f}$ with the set of analysing wavelets $\psi_{a,b}$

$$f(x) = \frac{1}{C_\psi} \int_{\mathbb{R}^+} \int_{\mathbb{R}} \widetilde{f}(a, b) \psi_{a,b}(x) \, \frac{\mathrm{d}a \, \mathrm{d}b}{a^2}, \qquad (2.3)$$

where $C_\psi = \int_{\mathbb{R}^+} |\hat{\psi}(k)|^2 k^{-1} \, \mathrm{d}k$ is a constant that depends on the wavelet ψ. Similarly to the Fourier transform, the wavelet transform corresponds to a change of basis (from physical space to wavelet space) and, since it is an isometry, it preserves the inner product ($\langle f, g \rangle = \langle \widetilde{f}, \widetilde{g} \rangle$) (Plancherel's theorem) and conserves energy (Parseval's identity), therefore

$$\int_{\mathbb{R}} |f(x)|^2 \, \mathrm{d}x = \frac{1}{C_\psi} \int_{\mathbb{R}^+} \int_{\mathbb{R}} |\widetilde{f}(a, b)|^2 \, \frac{\mathrm{d}a \, \mathrm{d}b}{a^2}. \qquad (2.4)$$

Note that the wavelet coefficients of the continuous wavelet transform are redundant and therefore correlated. This could be illustrated by the patterns one observes within the continuous wavelet coefficients of white noise, which correspond to the correlation between the dilated and translated wavelets (white noise being decorrelated by construction), which visualise the 'reproducing kernel' of the continuous wavelet transform. Due to the fact that wavelets are well localized in physical space, the behaviour of the signal at infinity does not play any role. Therefore both wavelet analysis and wavelet synthesis can be performed locally, in contrast to the Fourier transform which is intrinsically non-local (Fourier modes are spread all over space). One can also construct peculiar wavelets on a dyadic grid $\lambda = (j, i)$ (i.e. scale is sampled by octaves j and space by positions $2^{-j}i$) that are orthogonal to each other and are used to construct wavelet orthonormal bases. In contrast to the continuous wavelet coefficients equation (2.2) that are redundant and correlated, the orthogonal wavelet coefficients are decorrelated and non-redundant (i.e. a signal sampled on N points is perfectly represented by N orthogonal wavelet coefficients only). As for the Fourier transform, there exists a fast wavelet transform (FWT) that is even faster than the fast Fourier transform (FFT) whose operation count for a one-dimensional signal sampled at N points is proportional to N, instead of $N \log_2 N$ for the FFT.

2.1.2. *Orthogonal wavelet transform*

A discrete wavelet representation is obtained by sampling dyadically the scale a and the position b introducing $a_j = 2^{-j}$ and $b_{ji} = i a_j$ with $i, j \in \mathbb{Z}$. The resulting discrete wavelets

$$\psi_{ji}(x) = a_j^{-1/2} \psi \left(\frac{x - b_{ji}}{a_j} \right) = 2^{j/2} \psi (2^j x - i), \qquad (2.5)$$

generate orthogonal bases for peculiar wavelets. Figure 1 shows five discrete wavelets ψ_{ji} for $j = 3, \ldots, 7$ and their corresponding Fourier transforms, the modulus $|\widehat{\psi_{ji}}|$. Note that the scale 2^{-j} is related to the wavenumber k_j as
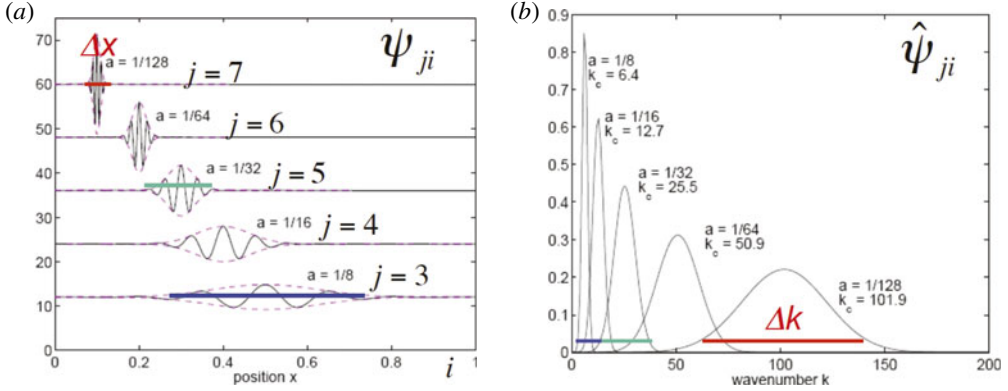
$$k_j = k_\psi 2^j, \qquad (2.6)$$

FIGURE 1. Wavelet representation. Physical space (*a*) and spectral space (*b*). Note that $\Delta x \Delta k > C$ is due to the Fourier uncertainty principle.

where $k_\psi = \int_0^\infty k |\hat{\psi}(k)| \, dk / \int_0^\infty |\hat{\psi}(k)| \, dk$ is the centroid wavenumber of the chosen wavelet. In figure 1 we observe the duality between physical and spectral space, namely small-scale wavelets are well localized in physical space and badly localized in spectral space, and *vice versa*. Denoting the support of a wavelet in physical space by Δx and the one in spectral space by Δk the Fourier uncertainty principle requires that the product $\Delta x \Delta k$ is bounded from below. In this case, the orthogonal wavelet coefficients of a function $f \in L^2(\mathbb{R})$ are given by

$$\widetilde{f}_{ji} = \langle f, \psi_{ji} \rangle, \tag{2.7}$$

and the corresponding orthogonal wavelet series reads

$$f(x) = \sum_{j,i \in \mathbb{Z}} \widetilde{f}_{ji} \psi_{ji}(x). \tag{2.8}$$

The integral in the continuous reconstruction forumla, (2.3), can thus be replaced by a discrete sum. In practical applications, the infinite sums of the wavelet series have to be truncated in both scale and position. Limiting the analysis to the largest accessible scale of the domain, $2^0 = L$, the scaling function associated to the wavelet has to be introduced and the wavelet series becomes

$$f(x) = \sum_{i \in \mathbb{Z}} \overline{f} \phi_{0i}(x) + \sum_{j \geqslant 0, i \in \mathbb{Z}} \widetilde{f}_{ji} \psi_{ji}(x), \tag{2.9}$$

where ϕ is the scaling function and $\overline{f} = \langle f, \phi_{0i} \rangle$ the corresponding scaling coefficients. The smallest scale 2^{-J} is given by the sampling rate of the function f, which determines the number of grid points $N = 2^J$. The finite domain size implies that the number of positions also becomes finite and, choosing $L = 1$, we obtain the range $i = 0, \ldots, 2^j - 1$ for $j = 0, \ldots, J - 1$. Figure 2 illustrates for an orthogonal spline wavelet the discrete scale-space representation for three different scales ($j = 6, 7, 8$) and positions. There exists a fast wavelet transform algorithm which computes the orthogonal wavelet coefficients in $O(N)$ operations, therefore it is even faster than the fast Fourier transform whose operation count is $O(N \log_2 N)$ (Mallat 1998).
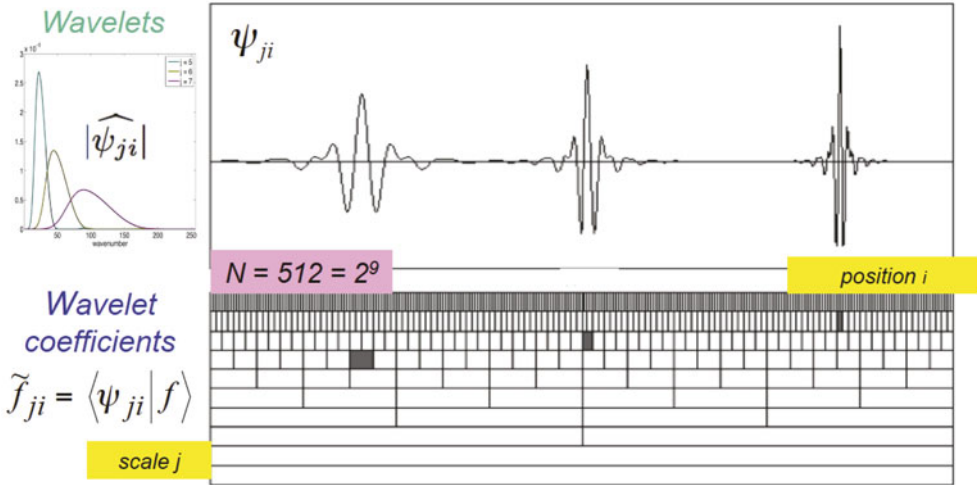
FIGURE 2. Space-scale representation of an orthogonal spline wavelet at three different scales and positions, i.e. $\psi_{6,6}, \psi_{7,32}, \psi_{8,108}$. The modulus of the Fourier transform of three corresponding wavelets is shown in the inset (top, left).
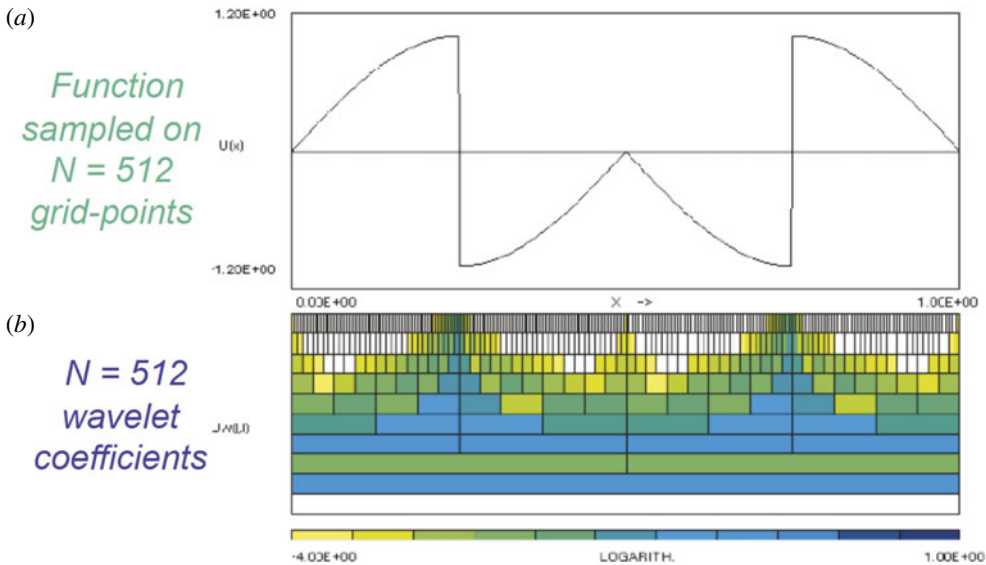

FIGURE 3. Academic example: function with two discontinuities and one in its derivative (*a*), corresponding modulus of orthogonal wavelet coefficients (*b*) in logarithmic scale using periodic spline wavelets of degree five.

As an example we show in figure 3 the orthogonal wavelet coefficients of an academic function presenting discontinuities. We observe that wavelet coefficients at small scales only have significant values in the vicinity of the discontinuities. Hence only a few coefficients are needed to represent the function after discarding the small wavelet coefficients.
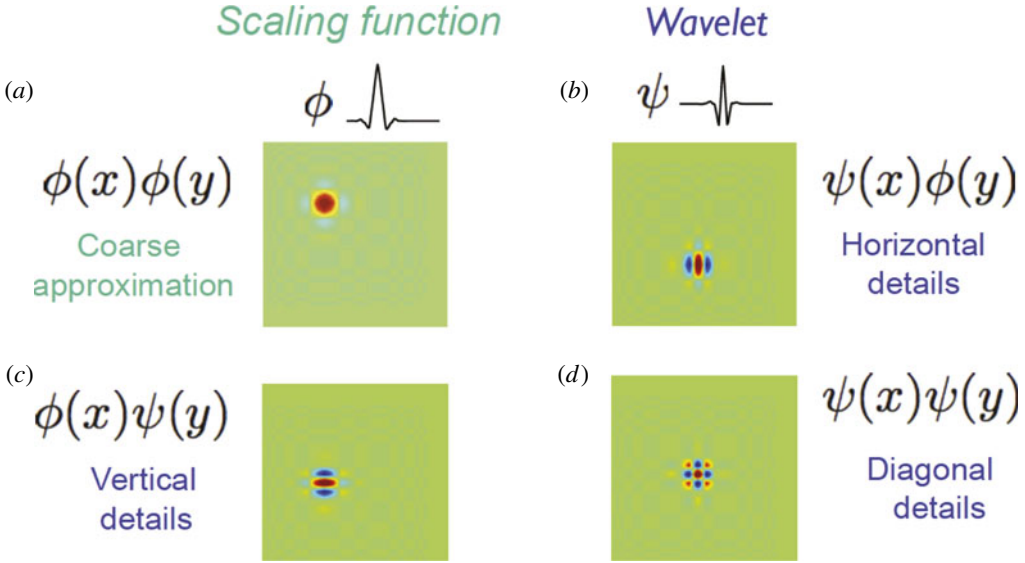
FIGURE 4. Two-dimensional orthogonal wavelets. Scaling function (*a*) and the three associated directional wavelets in the horizontal (*b*), vertical (*c*) and diagonal (*d*) direction.

Extension to higher dimensions. The orthogonal wavelet representation can be extended to represent functions in higher space dimensions using tensor product constructions, see e.g. Daubechies (1992), Mallat (1998), Schneider & Farge (2006). Figure 4 shows two-dimensional orthogonal wavelets constructed by tensor products.

The wavelet transform can also be generalized to treat vector-valued functions (e.g. velocity or magnetic fields) in d space dimensions by decomposing each vector component into an orthogonal wavelet series. In the following we consider a vector field $\boldsymbol{v} = (v^{(1)}, v^{(2)}, v^{(3)})$ for $d = 3$ sampled at resolution $N = 2^{3J}$ with periodic boundary conditions. Its orthogonal wavelet series reads

$$\boldsymbol{v}(\boldsymbol{x}) = \sum_{j=0}^{J-1} \sum_{\mu=1}^{7} \sum_{i_1,i_2,i_3=0}^{2^j-1} \widetilde{\boldsymbol{v}}_{j,\mu,\boldsymbol{i}} \psi_{j,\mu,\boldsymbol{i}}(\boldsymbol{x}), \tag{2.10}$$

using three-dimensional orthogonal wavelets $\psi_{j,\mu,\boldsymbol{i}}(\boldsymbol{x})$. The basis functions are constructed by tensor products of a set of one-dimensional wavelets and scaling functions (Daubechies 1992; Mallat 1998) which have been periodized since the boundary conditions considered here are periodic. The scale index j varies from 0 to $J - 1$, the spatial index $\boldsymbol{i} = (i_1, i_2, i_3)$ has 2^{3j} values for each scale 2^{-j} and each angle indexed by $\mu = 1, \ldots, 7$. The three Cartesian directions $\boldsymbol{x} = x^{(1)}, x^{(2)}, x^{(3)}$ correspond to $\mu = 1, 2, 3$, while $\mu = 4, 5, 6, 7$ denote the remaining diagonal directions. The wavelet coefficients measure the fluctuations of $\boldsymbol{v}$ at scale 2^{-j} and around position $2^{-j}\boldsymbol{i}$ for each of the seven possible directions μ. The contribution of the vector field $\boldsymbol{v}$ at scale 2^{-j} and direction μ can be reconstructed by summation of $\widetilde{\boldsymbol{v}}_{j,\mu,\boldsymbol{i}} \psi_{j,\mu,\boldsymbol{i}}(\boldsymbol{x})$ over all positions $\boldsymbol{i}$:

$$\boldsymbol{v}_{j,\mu}(\boldsymbol{x}) = \sum_{i_1,i_2,i_3=0}^{2^j-1} \widetilde{\boldsymbol{v}}_{j,\mu,\boldsymbol{i}} \psi_{j,\mu,\boldsymbol{i}}(\boldsymbol{x}). \tag{2.11}$$

The contribution of $\boldsymbol{v}$ at scale 2^{-j} is obtained by

$$\boldsymbol{v}_j(\boldsymbol{x}) = \sum_{\mu=1}^{7} \boldsymbol{v}_{j,\mu}(\boldsymbol{x}). \qquad (2.12)$$

For more details on wavelets, we refer the reader to several review articles, e.g. Farge (1992), Farge & Schneider (2006), Schneider & Farge (2006), Schneider & Vasilyev (2010) and textbooks, e.g. Daubechies (1992), Mallat (1998).

2.2. *Wavelet-based statistical diagnostics*

The physical representation gives access to both position and direction, the latter when the space dimension is larger than one. The spectral representation gives access to both wavenumber and direction, when the space dimension is larger than one, but the information on position is spread among the phases of all Fourier coefficients. The wavelet representation combines the advantages of both representations, while also giving access to scale. For instance, if we consider a three-dimensional vector-valued field, its orthogonal wavelet coefficients for each of its three components are indexed by three positions, seven directions and one scale. Thus using the wavelet representation, new statistical diagnostics can be designed by computing moments of coefficients using summation, either over position, direction or scale, or any combination of these. Second-order moments correspond to energy distributions (e.g. the energy spectrum), while higher-order moments allow for the computation of skewness and flatness. In the following, we will present scale-dependent moments, scale-dependent directional statistics and scale-dependent topological statistics. By topological statistics we mean the statistics of bilinear quantities, such as the scalar product of a vector field and its curl, e.g. helicity.

In the following, we give a summary of statistical diagnostics based on orthogonal wavelet analysis, here applied to a generic vector field following the lines of Okamoto *et al.* (2014). Decomposing a vector field into orthogonal wavelets, scale-dependent distributions of turbulent flows can be measured, including different directions and also different flow components. For example, the energy and its spatial fluctuations can be quantified at different length scales and in different directions and hence longitudinal or transverse contributions can be determined. In the case of an imposed magnetic field, the contributions in the directions perpendicular or parallel to it can be distinguished. To this end, statistical quantities based on the wavelet representation can be introduced, and the scale-dependent anisotropy and the corresponding intermittency of MHD turbulence can be examined. Here we define intermittency as a departure from Gaussianity, which is reflected by increasing flatness when scale decreases. Sandborn (1959) introduced this definition in the context of boundary layer flows and for a historical overview on intermittency we refer to Schneider, Farge & Kevlahan (2004). Alternative definitions of intermittency can be found, e.g. in Frisch (1995), for example a steepening of the energy spectrum proposed by Kolmogorov (1962). In Kurien & Sreenivasan (2000, 2001) and Sorriso-Valvo *et al.* (2006) related techniques to quantify the anisotropy of the flow and its intermittency have been proposed. They used structure functions of either tensorial components or applied the SO3 decomposition, which is based on spherical harmonics. Structure functions which correspond to moments of increments can be directly linked to wavelet decompositions (see, e.g. Schneider *et al.* 2004). The increments are wavelet coefficients using the poor man's wavelet, i.e. the difference of two delta distributions, which has only one

vanishing moment, its mean value. This implies that the exponent of the detectable scaling laws is limited by the order of the structure function, and the scale selectivity is reduced as the frequency localization of the poor man's wavelet is rather bad. These drawbacks can be overcome using higher-order wavelets.

2.2.1. *Scale-dependent moments*

To study the scale-dependent directional statistics we consider the component v^ℓ with $\ell = 1, 2, 3$ of a generic vector field $\boldsymbol{v}$. First we define the qth-order moment of the scale-dependent vector $\boldsymbol{v}_j(\boldsymbol{x}) = (v_j^{(1)}, v_j^{(2)}, v_j^{(3)})$, which is here either the vector field at scale 2^{-j} and direction μ, $v_{j,\mu}^{(\ell)}$, or the vector field at scale 2^{-j}, $v_j^{(\ell)}$,

$$M_q[v_j^{(\ell)}] = \langle (v_j^{(\ell)})^q \rangle. \tag{2.13}$$

By construction the mean value satisfies $\langle v_j^{(\ell)} \rangle = 0$ and hence the moments are automatically centred. These scale-dependent moments are related to the qth-order structure functions, as shown, e.g. in Schneider *et al.* (2004). In the following, we consider the second-order moment $M_2[v_j^{(\ell)}]$, which is a scale-dependent quadratic mean intensity of $v_j^{(\ell)}$, and the fourth-order moment $M_4[v_j^{(\ell)}]$, which contains the scale-dependent spatial fluctuations. Both moments are related via the flatness factor.

In anisotropic turbulence, typically a preferred direction can be defined, e.g. for low magnetic Reynolds number turbulence, or rotating turbulence. These flows have statistical symmetries, given here with respect to the x_3-axis. For the remaining perpendicular components, $\ell = 1, 2$, the average of these two components is taken as, $M_q[v_j^\perp] = \{M_q[v_j^{(1)}] + M_q[v_j^{(2)}]\}/2$, and the superscript $\perp$ represents the perpendicular contribution. The parallel contribution $v_j^{(3)}$ is denoted by $v_j^\parallel$.

The wavelet energy spectrum for $v_j^{(\ell)}$ is obtained using $M_2[v_j^{(\ell)}]$ and (2.6),

$$E[v_j^{(\ell)}] = \frac{1}{2\Delta k_j} M_2[v_j^{(\ell)}], \tag{2.14}$$

where $\Delta k_j = (k_{j+1} - k_j) \ln 2$ (Meneveau 1991; Addison 2002). It is thus directly related to the Fourier energy spectrum and yields a smoothed version (Meneveau 1991; Farge 1992). The orthogonality of the wavelets with respect to scale and direction guarantees that the total energy is obtained by direct summation, $E = \sum_{\ell,j} E[v_j^{(\ell)}] = \sum_{\ell,j,\mu} E[v_{j,\mu}^{(\ell)}]$.

The standard deviation of the energy spectrum at a given wavenumber k_j quantifies the spatial variability

$$\sigma[v_j^{(\ell)}] = \frac{1}{2\Delta k_j} \sqrt{M_4[v_j^{(\ell)}] - (M_2[v_j^{(\ell)}])^2}. \tag{2.15}$$

The ratio of the fourth- and second-order moments defines the scale-dependent flatness factor,

$$F[v_j^{(\ell)}] = \frac{M_4[v_j^{(\ell)}]}{(M_2[v_j^{(\ell)}])^2}, \tag{2.16}$$

which quantifies the flow intermittency at scale 2^{-j}.

The scale-dependent flatness is related to the energy spectrum (2.14) and the standard deviation (2.15),

$$F[v_j^{(\ell)}] = \left(\frac{\sigma[v_j^{(\ell)}]}{E[v_j^{(\ell)}]} \right)^2 + 1, \tag{2.17}$$

as shown in Bos, Liechtenstein & Schneider (2007). This relation illustrates that the spatial variability of the energy spectrum is directly reflected by the scale-dependent flatness.

2.2.2. *Scale-dependent directional statistics*

To quantify scale-dependent spatial flow anisotropy and anisotropic flow intermittency we introduce wavelet-based measures. Both component-wise anisotropy and directional anisotropy of the flow are considered in the following. For the scale-dependent mean energy, $E[v_j^{(\ell)}]$, the anisotropy measure can be defined similarly to the classical Fourier representation. Analogously, this can be extended for its spatial fluctuations, $\sigma[v_j^{(\ell)}]$. Using the relation between the scale-dependent flatness with the energy spectrum and its spatial fluctuations, (2.17), various measures of anisotropic flow intermittency can be defined.

Component-wise anisotropy. The scale-dependent component-wise anisotropy is defined by the ratio of perpendicular to parallel energy, and its fluctuation, at a given scale 2^{-j}, respectively,

$$c_E(k_j) = \frac{E[v_j^\perp]}{E[v_j^\parallel]}, \quad c_\sigma(k_j) = \frac{\sigma[v_j^\perp]}{\sigma[v_j^\parallel]}. \tag{2.18a,b}$$

The scale-dependent mean energy, $c_E(k_j)$ is a smoothed version of the Fourier counterpart $c(k)$. The component-wise anisotropy of the spatial fluctuations is quantified by $c_\sigma(k_j)$. These measures are directly related to the component-wise flatness factors of $v_j^{(\ell)}$, i.e. $F[v_j^\perp]$ and $F[v_j^\parallel]$, as shown in Okamoto *et al.* (2014). Combining (2.17) and (2.18) results in

$$\Lambda_j^C \equiv \left\{ \frac{c_\sigma(k_j)}{c_E(k_j)} \right\}^2 = \frac{F[v_j^\perp] - 1}{F[v_j^\parallel] - 1}, \tag{2.19}$$

which yields a scale-dependent measure of component-wise anisotropic intermittency.

Directional anisotropy. Scale-dependent measures for directional anisotropy can be defined using ratios of perpendicular to parallel energy and fluctuations in longitudinal or transverse directions,

$$d_E^L(k_j) = \frac{E[v_{j,L}^\perp]}{E[v_{j,L}^\parallel]}, \quad d_\sigma^L(k_j) = \frac{\sigma[v_{j,L}^\perp]}{\sigma[v_{j,L}^\parallel]}, \tag{2.20a,b}$$

$$d_E^T(k_j) = \frac{E[v_{j,3}^\perp]}{E[v_{j,T}^\perp]}, \quad d_\sigma^T(k_j) = \frac{\sigma[v_{j,3}^\perp]}{\sigma[v_{j,T}^\perp]}. \tag{2.21a,b}$$

The longitudinal direction is denoted by the index L, i.e. $L = \mu = \ell$. The subscript $\mu = 3$ corresponds to a transverse direction of the perpendicular components, while

T represents the other transverse direction of the perpendicular components, i.e. $T = \mu = 1$ for $v_{j,\mu}^{(2)}$ or $T = \mu = 2$ for $v_{j,\mu}^{(1)}$.

Three principal directions, i.e. $\mu = 1, 2$ and 3, out of the seven possible directions have been selected for the directional statistics.

The measures $d_E^L(k_j)$ and $d_E^T(k_j)$ are smoothed versions of the Fourier representation $2e^{(3)}(k_3)/\{e^{(1)}(k_1) + e^{(2)}(k_2)\}$ and $\{e^{(1)}(k_3) + e^{(2)}(k_3)\}/\{e^{(1)}(k_2) + e^{(2)}(k_1)\}$, respectively, following the interpretation of the directional statistics proposed in Bos *et al.* (2007). Furthermore, these quantities can be related to second-order structure functions defined in physical space, and we have:

$$\frac{2D^{(3)}(r\hat{l}_3)}{\{D^{(1)}(r\hat{l}_1) + D^{(2)}(r\hat{l}_2)\}} \quad \text{and} \quad \frac{\{D^{(1)}(r\hat{l}_3) + D^{(2)}(r\hat{l}_3)\}}{\{D^{(1)}(r\hat{l}_2) + D^{(2)}(r\hat{l}_1)\}}. \tag{2.22a,b}$$

Structure functions are defined as the spatial average of velocity increments, $D^{(\ell)}(r) = \langle \{v^{(\ell)}(x + r) - v^{(\ell)}(x)\}^2 \rangle$. Here $v^{(\ell)}$ consists of contributions of $v^{(\ell)}$ to scales larger than 2^{-j}. which are obtained by low pass filtering using the three-dimensional scaling function at scale 2^{-j}. The unit vector of the Cartesian direction x_ℓ is denoted by $\hat{l}_\ell$.

Combining (2.17) and (2.20)–(2.21), yields directional anisotropy measures (Okamoto *et al.* 2014):

$$\Lambda_j^L \equiv \left\{ \frac{d_\sigma^L(k_j)}{d_E^L(k_j)} \right\}^2 = \frac{F[v_{j,L}^\perp] - 1}{F[v_{j,L}^\parallel] - 1}, \tag{2.23}$$

$$\Lambda_j^T \equiv \left\{ \frac{d_\sigma^T(k_j)}{d_E^T(k_j)} \right\}^2 = \frac{F[v_{j,3}^\perp] - 1}{F[v_{j,T}^\perp] - 1}, \tag{2.24}$$

which quantify the scale-dependent anisotropic intermittency in the transverse and longitudinal directions. They measure intermittency, not only in the plane perpendicular or in the direction parallel to for example a magnetic field B_0, but also in the longitudinal or transverse directions. These measures are equal to one for isotropic fields, and their departure from the value one indicates the degree of flow anisotropy.

2.2.3. *Scale-dependent topological statistics*

Considering the velocity field u and the corresponding vorticity $\omega = \nabla \times u$, the kinetic helicity, $H(x) = u \cdot \omega$, can be defined. The helicity yields a measure of the geometrical statistics of turbulence. Integrating the helicity over space one obtains the mean helicity $\overline{H} = \langle u \cdot \omega \rangle$. The scale-dependent helicity H_j was introduced in Yoshimatsu *et al.* (2009*a*) and is defined by

$$H_j(x) = u_j \cdot \omega_j. \tag{2.25}$$

It preserves Galilean invariance, though the kinetic helicity itself does not. The corresponding mean helicity is obtained by summing H_j over scale, $\overline{H} = \sum_j \langle H_j \rangle$ due to the orthogonality of the wavelet decomposition.

The relative helicity

$$h(x) = \frac{H}{|u|\,|\omega|} \tag{2.26}$$

defines the cosine of the angle between the velocity and the vorticity at each spatial position. The range of h lies between -1 and $+1$. The scale-dependent relative helicity can be defined correspondingly

$$h_j(\boldsymbol{x}) = \frac{H_j}{|\boldsymbol{u}_j|\,|\boldsymbol{\omega}_j|}. \tag{2.27}$$

The Euler equations of hydrodynamics conserve the mean kinetic helicity, while in ideal MHD turbulence, the mean cross-helicity $\overline{H}^C = \langle \boldsymbol{u} \cdot \boldsymbol{b} \rangle$ and the mean magnetic helicity $\overline{H}^M = \langle \boldsymbol{a} \cdot \boldsymbol{b} \rangle$ are conserved quantities. Here $\boldsymbol{a}$ is the vector potential of the magnetic field $\boldsymbol{b}$. The scale-dependent versions of the relative cross and magnetic helicities have been introduced in Yoshimatsu *et al.* (2011) and are defined respectively by

$$h_j^C(\boldsymbol{x}) = \frac{H_j^C}{|\boldsymbol{u}_j||\boldsymbol{b}_j|}, \tag{2.28}$$

with $H^C(\boldsymbol{x}) = \boldsymbol{u} \cdot \boldsymbol{b}$ and

$$h_j^M(\boldsymbol{x}) = \frac{H_j^M}{|\boldsymbol{a}_j||\boldsymbol{b}_j|}, \tag{2.29}$$

with $H^M(\boldsymbol{x}) = \boldsymbol{a} \cdot \boldsymbol{b}$. These quantities define the cosine of the angle between the two vector fields.

2.3. *Application to three-dimensional MHD turbulence*

In the following, we show applications of the above scale-dependent wavelet-based measures to three-dimensional incompressible MHD turbulence. To study the anisotropy we analyse flows with a uniformly imposed magnetic field and consider the quasi-static (QS) approximation at moderate Reynolds numbers for different interaction parameters (Okamoto *et al.* 2011, 2014). For the geometrical statistics, full MHD turbulence without an imposed mean field is analysed (Yoshimatsu *et al.* 2011). The flows are computed by direct numerical simulation (DNS) with a Fourier pseudo-spectral method at resolution 512^3 and for further details we refer the reader to the two respective publications given above. The flow structure of the quasi-static MHD turbulence is illustrated in figure 5. Shown are isosurfaces of the modulus of vorticity for two different interaction parameters N. The interaction parameter characterizes the intensity of the imposed magnetic field B_0 (here chosen in the z direction) relative to the flow nonlinearity. It is defined by $N = \sigma B_0^2 L / \rho u'$, where σ is the electrical conductivity, L the integral length scale, ρ the density and u' the r.m.s. velocity. In the case without imposed magnetic field, i.e. $N = 0$, the flow is equivalent to isotropic hydrodynamic turbulence and entangled vortex turbes can be observed in figure 5(a). For $N = 2$, the structures are aligned parallel to the z direction, i.e. the direction of the imposed magnetic field, and the flow is thus strongly anisotropic.

The wavelet energy spectra (figure 6a) yield information on the kinetic energy at scale 2^{-j} and the spatial fluctuations are quantified by the standard deviation spectra (figure 6b). All spectra have been multiplied by $k^{5/3}$ to enhance their differences at small scale. We observe that the spectra decay with increasing normalized wavenumber $k_j\eta$ where η is the Kolmogorov length scale. Furthermore, the wavelet spectra (dotted lines) agree well with the corresponding Fourier spectra (solid lines). For larger values of N, the spectra $E[u_j^\perp]$ decay faster for increasing $k_j\eta$. The standard deviation spectra of $u_j^\perp$ also decay more rapidly when N becomes larger.
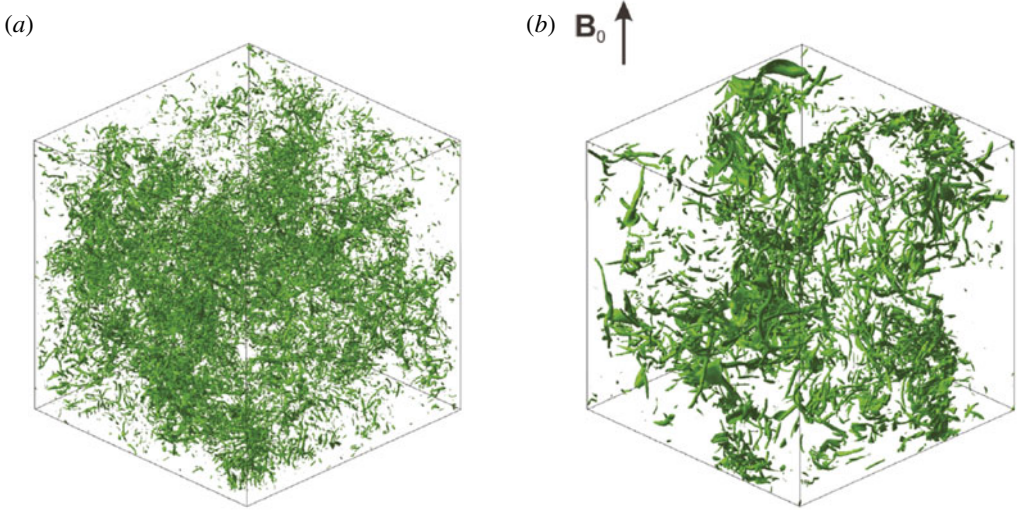
(a)   (b) $\mathbf{B}_0$ ↑

FIGURE 5. Quasi-static-three-dimensional-MHD: modulus of vorticity for quasi-static three-dimensional MHD at $R_\lambda = 235$, with $N = 0$, (a) and $N = 2$ (b) computed by DNS (from Okamoto *et al.* 2014).
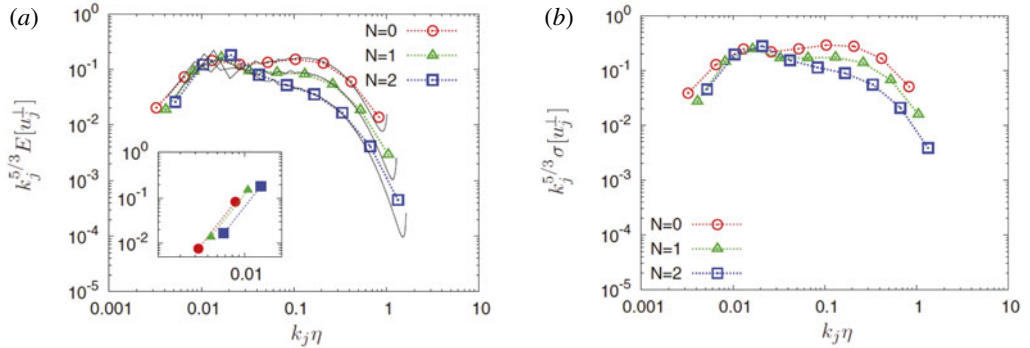
FIGURE 6. Quasi-static-three-dimensional-MHD: wavelet mean energy spectra (a) $k_j^{5/3} E^\perp(k_j)$ together with the Fourier energy spectra (solid lines). Wavelet standard deviation spectra (b) $k_j^{5/3} \sigma^\perp(k_j)$. All quantities are shown for the perpendicular velocity components. The inset (left) shows the corresponding forcing Fourier spectra $k^{5/3} E_f(k)$ (from Okamoto *et al.* 2014).

The scale-dependent anisotropy measures allow us to analyse the anisotropy at different scales. The scale-dependent component-wise anisotropy $c_E(k_j)$ shown in figure 7(a), quantifies the anisotropy of the wavelet mean energy spectrum. As expected, we find for $N = 0$ that $c_E(k_j) \approx 1$ as the flow is isotropic. The departure from the value one corresponds to flow anisotropy, i.e. for values smaller than one the energy of the parallel component is predominant over that of the perpendicular component, an observation which holds for both cases, $N = 1$ and $N = 2$. Furthermore, the anisotropy is persistent at the smaller scales and yields smaller values for $N = 2$. Now we examine the anisotropy in different directions. Figure 7(b), shows d_E^L, the flow anisotropy of the mean wavelet spectrum in the longitudinal direction. We find that this measure yields values larger than one for $N = 1$ and 2, and values close
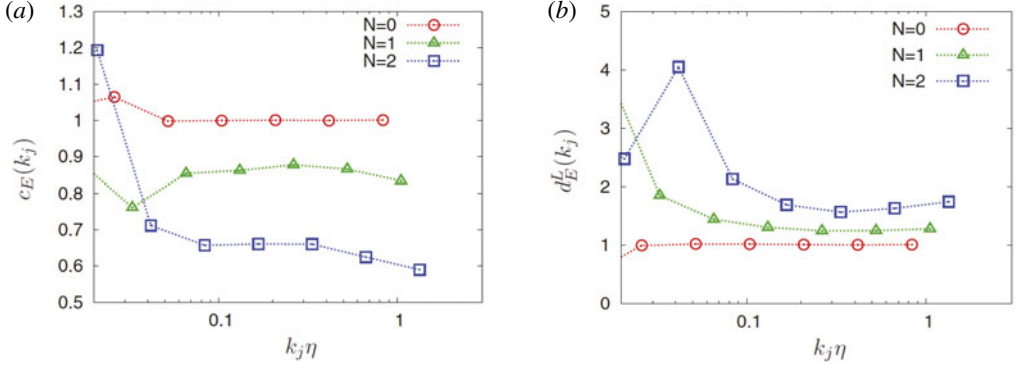
FIGURE 7. Quasi-static-three-dimensional-MHD: component-wise anisotropy measure $c_E(k_j)$ (a) and directional anisotropy measure in the longitudinal direction $d_E^L(k_j)$ (from Okamoto *et al.* 2014).
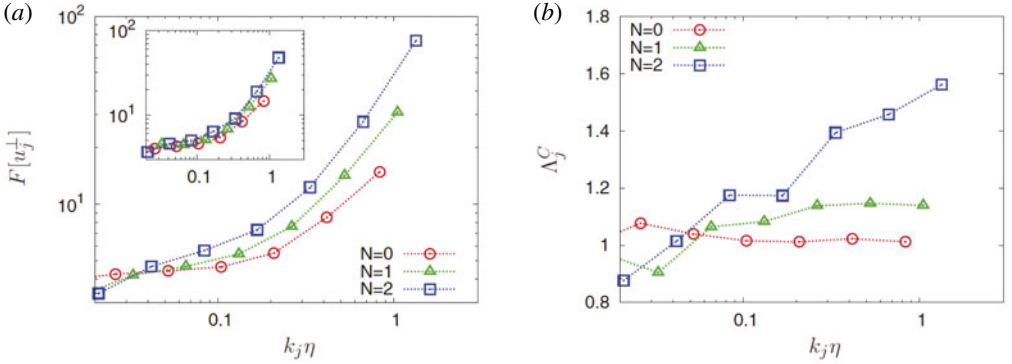

FIGURE 8. Quasi-static-three-dimensional-MHD: scale-dependent flatness of the perpendicular velocity $F_j^\perp$ with in the inset the corresponding flatness for the parallel velocity (a). Anisotropic measure of intermittency $\Lambda(k_j)$ (b) (from Okamoto *et al.* 2014).

to one for $N = 0$. For $N \neq 0$, the correlation of the velocity component parallel to the imposed magnetic field in its longitudinal direction is supposed to be stronger than the correlation of the perpendicular components. We also see that the scale dependence becomes weak for $k_j\eta > 0.1$.

The scale-dependent flatness of the perpendicular velocity $F[u_j^\perp]$ and of the parallel velocity $F[u_j^\parallel]$, shown in figure 8(a), quantify the intermittency of the different flow components. In all cases we find that the flatness does indeed increase for decreasing scale. At small scales, $k_j\eta > 1$, we also see that the flatness is larger for larger values of N. The inset shows that $F[u_j^\parallel]$ behaves similarly.

The component-wise anisotropy of the intermittency at each scale can be quantified with $\Lambda^C(k_j)$, see figure 8(b). Again we find that for $N = 0$ values close to one are found, as expected due to the isotropy of the flow. For $N = 1$ and 2 the component-wise anisotropic intermittency $\Lambda^C(k_j)$ has values larger than one for $k_j\eta > 0.1$, which means that the perpendicular velocity becomes more intermittent than the parallel velocity at small scales. For $N = 2$ this becomes even more pronounced.
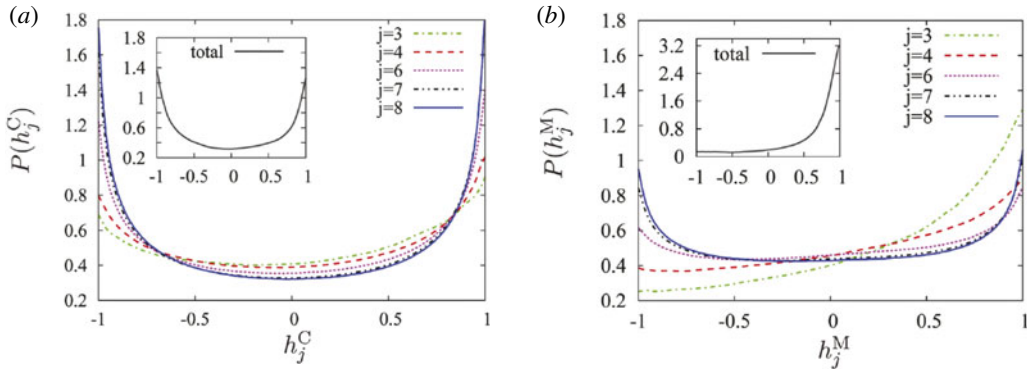
FIGURE 9. Three-dimensional-MHD: scale-dependent PDFs of the relative helicities. Cross-helicity h_j^C (a) and magnetic helicity h_j^M (b). The insets show the PDFs of the corresponding total relative helicities (from Yoshimatsu *et al.* 2011).

To illustrate the scale-dependent geometric statistics we consider homogeneous MHD turbulence at unit Prandtl number without mean magnetic field. The flow has been computed by direct numerical simulation at resolution 512^3 with random forcing and for further details we refer to Yoshimatsu *et al.* (2011). Figure 9 shows the probability distribution functions (PDFs) of the relative scale-dependent cross and magnetic helicity, h_j^C and h_j^M. Figure 9(a) exhibits two peaks at $h_j^C = \pm 1$ which corresponds to a pronounced scale-dependent dynamic alignment. The peaks even become larger for smaller scales and thus the probability of alignment (or anti-alignment) of the velocity and the magnetic field increases. Figure 9(b) illustrates that the distribution of the scale-dependent magnetic helicity becomes more symmetric at small scales. The inset shows that the total relative magnetic helicity is strongly skewed with a peak at $+1$, which is due to the presence of substantial mean magnetic helicity.

3. Extraction of coherent structures using wavelets

In this section we illustrate the extraction of coherent structures using an algorithm which is based on wavelet denoising (Farge, Schneider & Kevlahan 1999; Farge, Pellegrino & Schneider 2001; Farge *et al.* 2003; Azzalini, Farge & Schneider 2005). We first describe it for one-dimensional scalar-valued signals and illustrate its performance on an academic test signal. We then generalize the algorithm to higher dimensions and to vector-valued fields. Finally, different applications to experimental and numerical data are shown:

 (i) a scalar-valued signal varying in time measured by a Langmuir probe in the scrape-off layer of the tokamak Tore Supra (Cadarache, France);
 (ii) a two-dimensional academic example of the synthetic emissivity of a radiating toric shell with additive noise;
(iii) experimental movies obtained by a fast camera implemented in Tore Supra;
(iv) two-dimensional vorticity fields computed for resistive drift-wave turbulence (Hasegawa–Wakatani model) using a pseudo-spectral method;
 (v) three-dimensional vorticity and current density fields computed for resistive MHD turbulence (incompressible MHD equations) using a pseudo-spectral method.

3.1. *Extraction algorithm*

3.1.1. *Principle*

We propose a wavelet-based method to extract coherent structures that emerge out of turbulent flows, both in fluids (e.g. vortices, shock waves in compressible fluids, . . .) and in plasmas (e.g. bursts, blobs, . . .). The goal is to study their role regarding the transport and mixing properties of flows in the turbulent regime.

For this, we use the wavelet representation that keeps track of both time and scale, instead of the Fourier representation that keeps track of frequency only. Since there is not yet an universal definition of the coherent structures encountered in turbulent flows, we use an apophatic method (introduced in Hinduist theology several thousands years ago) where one does not try to define what an entity (e.g. a phenomenon, a noumenon, . . .) is but rather what it is not. We thus agree on the minimal and hopefully consensual statement: 'coherent structures are not noise', and propose to define them as: 'coherent structures are what remains after denoising'.

The mathematical definition of noise states that a signal is noise if it cannot be compressed in any functional basis. As a result, the shortest description of a noise is itself. Note that in most of the cases, the experimental noise generated by a measurement device does not fit the definition of mathematical noise since it can be compressed in at least one functional basis (e.g. parasite frequencies can be removed in the Fourier basis).

This new way of defining coherent structures allows us to process signals and fields and also their cuts or projections (e.g. a probe located at one point provides a one-dimensional cut of a four-dimensional space-time field). Indeed, the algorithms commonly used to extract coherent structures cannot work for cuts or projections because they require a template of the structures to extract (one would need to take into account of how the probe sees all possible translations and distortions of the coherent structures). The strength of our algorithm is that it treats fields and projections in the same way.

Since we assume that coherent structures are what remains after denoising, we need a model, not for the structures themselves, but for the noise. Applying 'Ockham's Razor principle' (or the 'law of parsimony'), we choose as a first guess the simplest possible model: we suppose the noise to be additive, Gaussian and white (i.e. uncorrelated). We then project the turbulent signal (in one-dimension), or turbulent field (in higher dimensions), into wavelet space and retain only the coefficients having a modulus larger than a given threshold. As a threshold value we follow Donoho and Johnstone's proposition of a threshold value that depends on the variance of the Gaussian noise we want to remove and on the chosen sampling rate (Donoho & Johnstone 1994). Since the noise variance is not known *a priori* for turbulent signals (the noise being produced by their intrinsic nonlinear dynamics), we designed a recursive method Azzalini *et al.* (2005) to estimate it from the variance of the weakest wavelet coefficients, i.e. those whose modulus is below the threshold value. After applying our algorithm, we obtain two orthogonal fields: the coherent field retaining all coherent structures and the incoherent field corresponding to the noise. We then check *a posteriori* that the latter is indeed noise-like (i.e. spread all over physical space), Gaussian and uncorrelated (i.e. also spread all over Fourier space), and thus confirm the hypotheses we have *a priori* chosen for the noise.

3.1.2. *Wavelet denoising*

We consider a signal $s(t)$ sampled on $N = 2^J$ points that we want to denoise, assuming the noise to be additive, Gaussian and white. We first project $s(t)$ onto an

orthogonal wavelet basis and then filter out some of the wavelet coefficients thus obtained, $\widetilde{s}_{ij}$. We retain only the wavelet coefficients whose modulus is larger than a threshold value. The main difficulty is to estimate it *a priori* and we encounter two possible cases:

(i) If we *a priori* know the noise's variance σ^2, the optimal threshold value is given by Donoho and Johnstone's formula (Donoho & Johnstone 1994)

$$\epsilon = (2\sigma^2 \ln N)^{1/2}. \qquad (3.1)$$

In 1994 they proved (Donoho & Johnstone 1994) that such a wavelet thresholding method is optimal to denoise signals in the presence of additive Gaussian white noise because it minimizes the maximal L^2-error (between the denoised signal and the noise-free signal) for functions whose regularity is inhomogeneous, such as bursty or intermittent turbulent signals.

(ii) If we do not *a priori* know the variance of the noise, which is the most usual case, one should use the wavelet-based recursive algorithm we proposed in Farge *et al.* (1999), Azzalini *et al.* (2005). This algorithm first estimates the variance of the noise by considering the variance of the noisy signal σ_0^2 and computes the corresponding threshold

$$\epsilon_0 = (2\sigma_0^2 \ln N)^{1/2}. \qquad (3.2)$$

The algorithm splits the wavelet coefficients into two classes: the weak coefficients whose moduli are smaller than the threshold, and the remaining strong coefficients. It then computes the variance of the weak coefficients σ_n to obtain a better estimation of the variance of the noise (estimated from the wavelet coefficients using Parseval's theorem)

$$\sigma_n^2 = \frac{1}{N} \sum_{(j,i)\in\mathcal{I}^J, |\widetilde{s}_{ji}|<\epsilon_n} |\widetilde{s}_{ji}|^2, \qquad (3.3)$$

where $\mathcal{I}^J = \{0 \leqslant j < J, i = 0, \ldots, 2^j - 1\}$ is the index set of the wavelet coefficients. The algorithm then replaces ϵ_0 by $\epsilon_n = (2\sigma_n^2 \ln N)^{1/2}$, which yields a better estimate of the threshold. This procedure is iterated until it reaches the optimal threshold value, when $\epsilon_{n+1} \approx \epsilon_n$.

In Azzalini *et al.* (2005) we proved that this algorithm converges for signals having a sufficiently sparse representation in wavelet space, such as the intermittent signals encountered in turbulence. We also showed that the larger the signal to noise ratio (SNR) is, the faster the convergence. Hence, if the signal $s(t)$ is only noise, it converges in one iteration and retains ϵ_0 as the optimal threshold.

Using the optimal threshold, we then separate the wavelet coefficients $\widetilde{s}_{ij}$ into two contributions: the coherent coefficients $\widetilde{s}_{ij}^C$ whose moduli are larger than ϵ and the remaining incoherent coefficients $\widetilde{s}_{ij}^I$. Finally, the coherent component $s^C(t)$ is reconstructed in physical space using the inverse wavelet transform, while the incoherent component is obtained as $s^I(t) = s(t) - s^C(t)$.

3.1.3. *Extraction algorithm for one-dimensional signals*

We detail the iterative extraction algorithm for the one-dimensional case and quote it from Azzalini *et al.* (2005):

Initialization

(i) given the signal $s(t)$ of duration T, sampled on an equidistant grid $t_i = iT/N$ for $i = 0, N - 1$, with $N = 2^J$;

(ii) set $n = 0$ and perform a wavelet decomposition, i.e. apply the FWT (Mallat 1998) to s to obtain the wavelet coefficients $\widetilde{s}_{ji}$ for $(j, i) \in \mathcal{I}^J$;

(iii) compute the variance σ_0^2 of s as a rough estimate of the variance of the incoherent signal s^I and compute the corresponding threshold $\epsilon_0 = (2 \ln N \sigma_0^2)^{1/2}$, where $\sigma_0^2 = (1/N) \sum_{(j,i) \in \mathcal{I}^J} |\widetilde{s}_{ji}|^2$;

(iv) set the number of coefficients considered as noise to $N_I = N$, i.e. to the total number of wavelet coefficients.

Main loop

Repeat

(i) set $N_I^{old} = N_I$ and count the number of wavelet coefficients smaller than ϵ_n, which yields a new value for N_I;

(ii) compute the new variance σ_{n+1}^2 from the wavelet coefficiens smaller than ϵ_n, i.e. $\sigma_{n+1}^2 = (1/N) \sum_{(j,i) \in \mathcal{I}^J} |\widetilde{s}_{ji}^I|^2$, where

$$\widetilde{s}_{ji}^I = \begin{cases} \widetilde{s}_{ji} & \text{for } |\widetilde{s}_{ji}| \leqslant \epsilon_n \\ 0 & \text{else} \end{cases} \tag{3.4}$$

and the new threshold $\epsilon_{n+1} = (2 \ln N \sigma_{n+1}^2)^{1/2}$;

(iii) set $n = n + 1$

until $(N_I = N_I^{old})$.

Final step

(i) reconstruct the coherent signal s^C from the coefficients $\widetilde{s}_{ji}^C$ using the inverse FWT, where

$$\widetilde{s}_{ji}^C = \begin{cases} \widetilde{s}_{ji} & \text{for } |\widetilde{s}_{ji}| > \epsilon_n \\ 0 & \text{else} \end{cases} \tag{3.5}$$

(ii) finally, compute pointwise the incoherent signal $s^I(t_i) = s(t_i) - s^C(t_i)$ for $i = 0, \ldots, N - 1$.

End

Note that the signal is split into $s(t) = s^C(t) + s^I(t)$ and its energy into $\sigma^2 = \sigma_C^2 + \sigma_I^2$, since the coherent and incoherent components are orthogonal, i.e. $\langle s^C, s^I \rangle = 0$.

We use the FWT (Mallat 1998) that is computed with $(2MN)$ multiplications, M being the length of the discrete filter defining the orthogonal wavelet used. Remark: for all applications presented in this paper, we use Coiflet 12 wavelets (Daubechies 1992), unless otherwise stated. As long as the filter length $M < (\log_2 N)/2$, the FWT is faster than the FFT computed with $N \log_2 N$ operations. Consequently, the extraction algorithm requires $(2nMN)$ operations, n being the number of iterations, which is small, typically less than $\log_2 N$.

This algorithm defines a sequence of estimated thresholds $(\epsilon_n)_{n\in\mathbb{N}}$ and the corresponding sequence of estimated variances $(\sigma_n^2)_{n\in\mathbb{N}}$. In Azzalini *et al.* (2005) we proved that this sequence converges after a finite number of iterations by applying a fixed point type argument to the iteration function

$$\mathcal{F}_{s,N}(\epsilon_{n+1}) = \left(\frac{2\ln N}{N} \sum_{(j,i)\in\mathcal{I}^J} |\widetilde{s}_{ji}^I(\epsilon_n)|^2 \right)^{1/2}. \tag{3.6}$$

The algorithm stops after n iterations, when $\mathcal{F}_{s,N}(\epsilon_n) = \epsilon_{n+1}$, since the number of samples N is finite. In Azzalini *et al.* (2005) we also proved that the convergence rate depends on the SNR (SNR $= 10\log_{10}(\sigma^2/\sigma_I^2)$), since the smaller the SNR, i.e. the stronger the noise, the faster the convergence, moreover, if the algorithm is applied to a Gaussian white noise, it converges in one iteration only. If it is applied to a signal without noise, the signal is fully preserved. In Azzalini *et al.* (2005) we have also proven the algorithm's idempotence, i.e. if it is applied several times the noise is eliminated the first time and the coherent signal will remain the same if the algorithm is reapplied several times. This would be the case for a Gaussian filter which, in contrast, is not idempotent.

3.1.4. *Application to an academic test signal*

To illustrate the performance of the iterative algorithm we consider a one-dimensional noisy test signal $s(t)$ sampled on $N = 2^{13} = 8192$ points (figure 10*b*). It is made by adding a Gaussian white noise $w(t)$, of mean zero and variance $\sigma_w^2 = 25$, to a piecewise regular academic signal $a(t)$ presenting several discontinuities, in the function or in its derivatives (figure 10*a*). The SNR is SNR $= 10\log_{10}(\sigma_a^2/\sigma_w^2) = 11$ dB. After applying the extraction algorithm we estimate the noise variance to be 25.6 and we obtain a coherent signal $s^C(t)$ very close to the original academic signal $a(t)$ (figure 10*c*). The incoherent part $s^I(t)$ is homogeneous and noise-like with flatness 3.03, which corresponds to quasi-Gaussianity. In figure 10(*c*) we observe that the coherent signal retains all discontinuities and peaks present in the academic signal $a(t)$, which is an advantage with respect to standard denoising techniques, e.g. low pass Fourier filtering, which smooth them. In the vicinity of the discontinuities we observe slight overshoots, which are more local than the classical Gibbs phenomena and could for example be removed using the translation invariant wavelet transform (Mallat 1998).

3.1.5. *Extension of the algorithm to higher dimensional scalar- and vector-valued fields*

The extraction algorithm was described in § 3.1.3 for one-dimensional scalar-valued signals $s(t)$ varying in time. First, it can be extended to higher dimensional scalar fields $s(\boldsymbol{x})$ varying in space $\boldsymbol{x} \in \mathbb{R}^d$ where d is the space dimension. To this end the extraction algorithm only requires that the one-dimensional wavelets are replaced by their equivalent d-dimensional wavelets using tensor product constructions, see, e.g. (Daubechies 1992; Mallat 1998; Schneider & Farge 2006).

Second, the extraction algorithm can also be extended to vector-valued fields $\boldsymbol{v} = (v^{(1)}, \ldots, v^{(d)})$ where each component v^ℓ, $\ell = 1, \ldots, d$ is a scalar valued field. The extraction algorithm is then applied to each component of the vector field. For thresholding the wavelet coefficients we consider the vector $\widetilde{\boldsymbol{v}}_{j,\mu,i}$ in (2.10). Assuming statistical isotropy of the noise, the modulus of the wavelet coefficient vector is
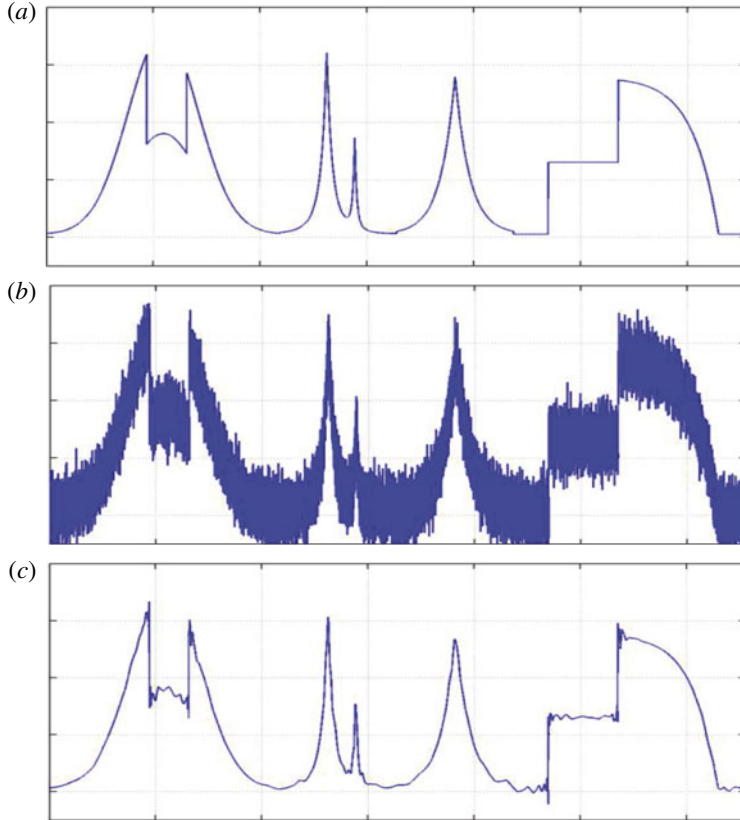
FIGURE 10. Denoising of a piecewise regular signal using iterative wavelet thresholding. (*a*) Original academic signal $a(t)$. (*b*) Noisy signal $s(t)$ with a SNR $= 11$ dB. (*c*) Denoised signal $s^C(t)$ with a SNR $= 28$ dB.

computed. The coherent contribution is then reconstructed from those coefficients whose modulus is larger than the threshold defined as $\epsilon = (2/d\,\sigma^2\ln N)^{1/2}$ where d is the dimensionality of the vector field, σ the variance of the noise and N the total number of grid points. The iterative algorithm in § 3.1.3 can then be applied in a straightforward way.

To extract coherent structures out of turbulent flows we consider the vorticity field, which is decomposed in wavelet space. Applying the extraction algorithm then yields two orthogonal components, the coherent and incoherent vorticity fields. Subsequently the corresponding induced velocity fields can be reconstructed by applying the Biot–Savart kernel, which is the inverse curl operator. For MHD turbulence, we consider in addition the current density and we likewise split it into two components, the coherent and incoherent current density fields. Using Biot–Savart's kernel we reconstruct the coherent and incoherent magnetic fields.

Note that the employed wavelet bases do not *a priori* constitute divergence-free bases. Thus the resulting coherent and incoherent vector fields are not necessarily divergence free. However, we checked that the departure from incompressibility only occurs in the dissipative range and remains negligible (Yoshimatsu *et al.* 2009*b*). Another solution would be to use directly div-free wavelets, however these are much more cumbersome to implement (Deriaz, Farge & Schneider 2010).
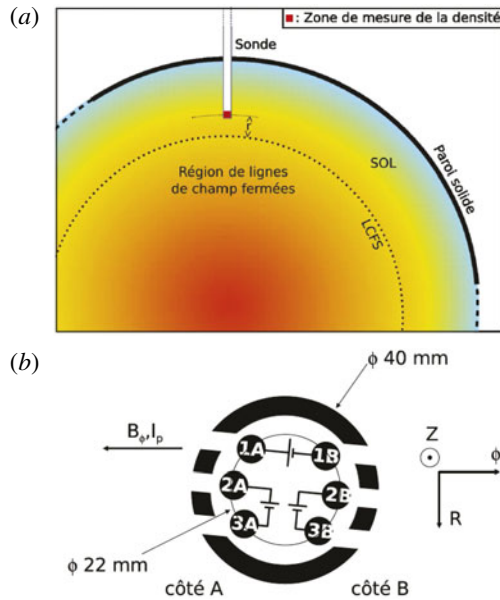
FIGURE 11. (*a*) Position of the reciprocating Langmuir probe in the scrape-off layer of the tokamak Tore Supra in Cadarache. (*b*) Schematic top view of the probe.

3.2. *Application to one-dimensional experimental signals from tokamaks*

In Farge, Schneider & Devynck (2006) we presented a new method to extract coherent bursts from turbulent signals. Ion density plasma fluctuations were measured by a fast reciprocating Langmuir probe in the scrape-off layer of the tokamak Tore Supra (Cadarache, France). For a schematic view we refer to figure 11. The resulting turbulent signal is shown in figure 12(*a*). To extract the coherent burst, the wavelet representation is used which keeps track of both time and scale and thus preserves the temporal structure of the analysed signal, in contrast to the Fourier representation which scrambles it among the phases of all Fourier coefficients. Applying the extraction algorithm described in § 3.1.3, the turbulent signal in figure 12(*a*) is decomposed into coherent and incoherent components (figure 12*b*,*c*). Both signals are orthogonal to each other and their properties can thus be studied independently. This procedure disentangles the coherent bursts, which contain most of the density variance, are intermittent and correlated with non-Gaussian statistics, from the incoherent background fluctuations, which are much weaker, non-intermittent, noise-like and almost decorrelated with quasi-Gaussian statistics.

The corresponding PDFs are shown in figure 13 which confirm that the incoherent part is indeed Gaussian like, while the total and coherent signal have similar skewed PDFs with algebraic heavy tails for positive signal values. Diagnostics based on the wavelet representation were also introduced in Farge *et al.* (2006) which allow us to compare the statistical properties of the original signals with their coherent and incoherent components. The wavelet spectra, in comparison with classical Fourier spectra (obtained via modified periodograms) in figure 14(*a*), confirm that the total and coherent signals have almost the same scale energy distribution with a power
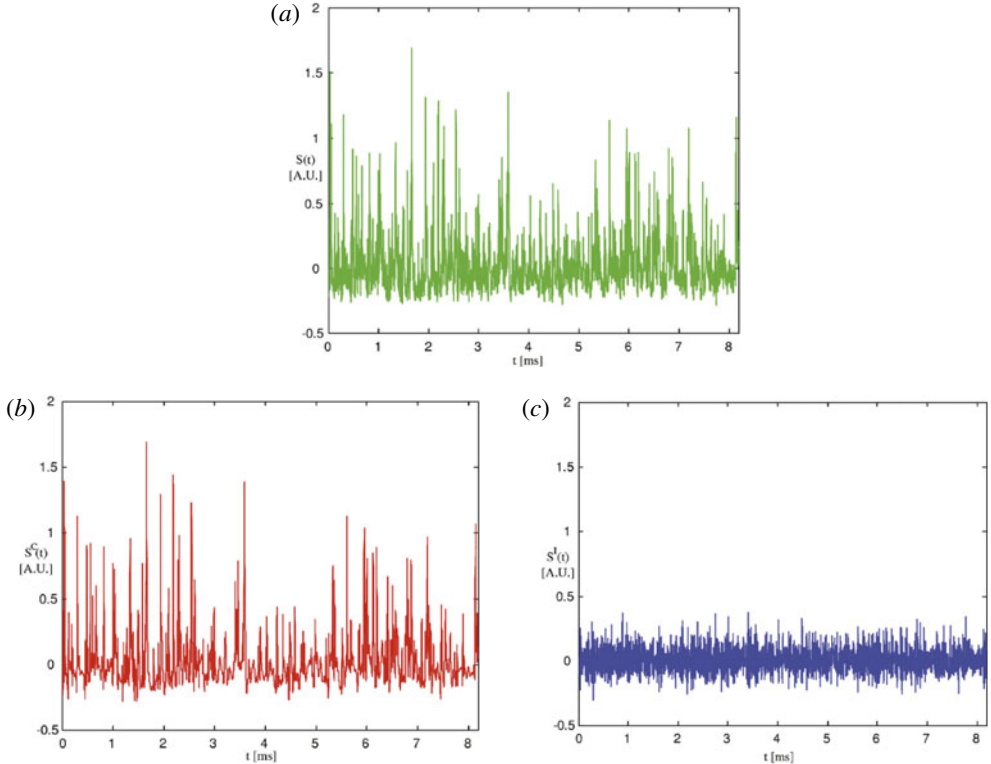
FIGURE 12. Signal $s(t)$ of duration 8.192 ms, corresponding to the saturation current fluctuations measured at 1 MHz in the scrape-off layer of the tokamak Tore Supra (Cadarache, France). (*a*) Total signal s, (*b*) coherent part s_C, and (*c*) incoherent part s_I (from Farge *et al.* 2006).

law behaviour close to $-5/3$. Furthermore, the wavelet spectra agree well with the Fourier spectra. The incoherent signal yields an energy equipartition for more than two magnitudes, which corresponds to decorelation in physical space. To quantify the intermittency we plot in figure 14(*b*) the scale-dependent flatness of the different signals, which shows that the coherent contribution extracted from the total signal has the largest values at small scale (i.e. high frequency) and is thus the most intermittent. In Farge *et al.* (2006) we conjectured that the coherent bursts are responsible for turbulent transport, whereas the remaining incoherent fluctuations only contribute to turbulent diffusion. This is confirmed by the resulting energy flux of the total, coherent and incoherent parts given in figure 15. Note that cross-correlation between coherent and incoherent contributions of the electric potential and the saturation current are not shown.

3.3. *Application to two-dimensional experimental movies from tokamaks*

3.3.1. *Tomographic reconstruction using wavelet-vaguelette decomposition*

Cameras installed in tokamaks acquire images which are difficult to interpret, since the three-dimensional structure of the plasma is mapped onto two spatial dimensions and thus flattened in a non-trivial way. This implies that the received flux cannot be directly related to the volumic emissivity of the plasma, which is a major limitation of
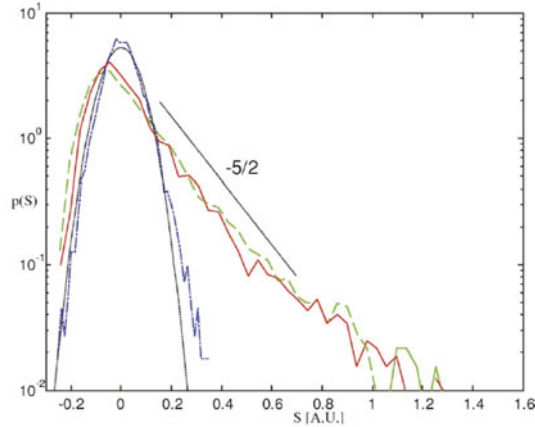
FIGURE 13. Probability density function $p(s)$ estimated using histograms with 50 bins. PDF of the total signal s (green dashed line), of the coherent component s_C (red solid line) and of the incoherent component s_I (blue dotted line), together with a Gaussian fit with variance σ_I^2 (black dotted line) (from Farge *et al.* 2006).
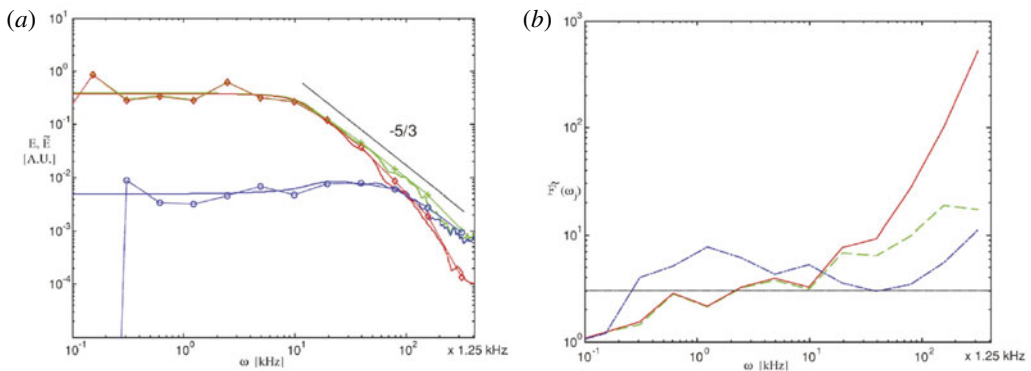

FIGURE 14. (*a*) Wavelet spectra $\widetilde{E}(\omega_j)$ (lines with symbols) and modified periodograms $E(\omega)$ (lines) of the total signal s (green and $+$), coherent signal s_C (red and $\diamond$) and incoherent signal s_I (blue and $\bigcirc$). (*b*) Corresponding scale-dependent flatness $\widetilde{F}$ versus frequency ω_j. The horizontal dotted line $\widetilde{F}(\omega_j) = 3$ corresponds to the flatness of a Gaussian process (from Farge *et al.* 2006).

such optical diagnostics. The reason is that the photons collected by each pixel on the camera sensor have been emitted along a corresponding ray, rather than out of a single point in space. Nevertheless the three-dimensional radiation can be related to the two-dimensional image using tomographic reconstruction, because the dominant structures in tokamak edge turbulence happen to be field-aligned filaments, commonly known as blobs. They have a higher density than their surroundings, and their structure varies more slowly along magnetic field lines than in their orthogonal directions.

Mathematically, the tomographic reconstruction corresponds to an inverse problem which has a formal solution under the assumed symmetry, but is ill-posed in the presence of noise. Taking advantage of the slow variation of the fluctuations along magnetic field lines in tokamaks, this inverse problem can be modelled by a helical
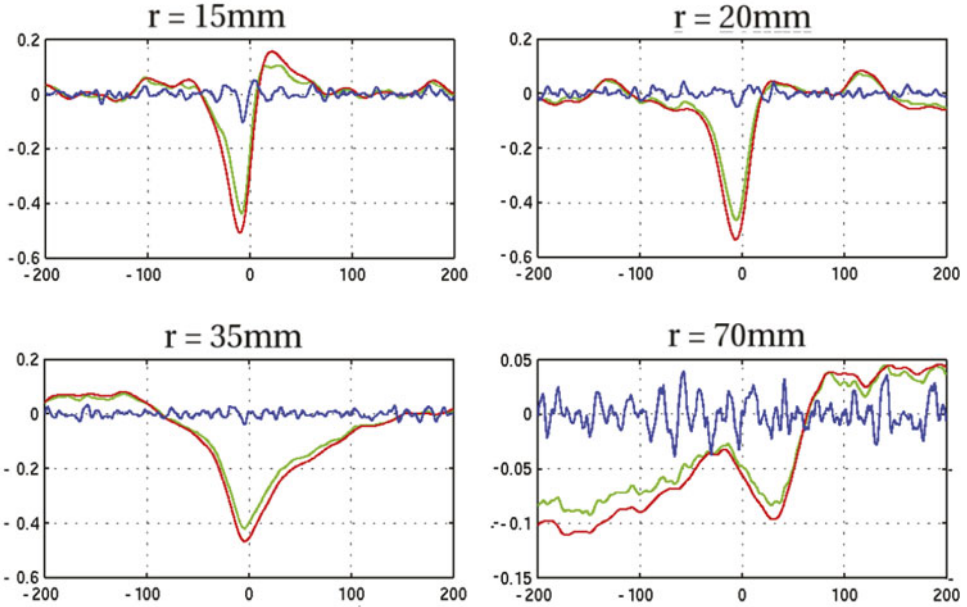
FIGURE 15. Energy flux: total (green), coherent (red) and incoherent (blue). The split is made using complex valued wavelets.

Abel transform, which is a Volterra integral operator of the first kind. In Nguyen van yen *et al.* (2012) we proposed a tomographic inversion technique, based on a wavelet-vaguelette decomposition coupled with wavelet denoising, to extract coherent structures which allows us to detect individual blobs on the projected movie and to analyse their behaviour. The wavelet-vaguelette decomposition (WVD) was introduced by Tchamitchian (1987) and used by Donoho (1995) to solve inverse problems in the presence of localized structures. Tomographic inversion using the wavelet-vaguelette decomposition is as an alternative to singular value decomposition (SVD). Both decompositions regularize the problem by damping the modes of the inverse transform to prevent amplification of the noise, i.e. modes below a given threshold are eliminated. For WVD, the nonlinear iterative thresholding procedure (see § 3.1.3) is applied to the vaguelette coefficients. Here Coiflets with two vanishing moments are used (Daubechies 1992). However, in contrast to SVD, WVD takes in addition advantage of the spatial localization of coherent structures present in the plasma.

   The technicalities of WVD are described in detail in Nguyen van yen *et al.* (2012), in the following we explain only the principle. The helical Abel transform related the plasma light emissivity S (a scalar-valued field) to the integral of the volume emissivity received by the camera $I = KS$, where K is a compact continuous operator. The reconstruction of the plasma light emissivity S from I is an inverse problem which becomes very difficult when S is corrupted by noise, since computing K^{-1} is an ill-posed problem which amplifies the noise. The vaguelettes are operator adapted wavelets and a biorthogonal set of basis functions is obtained from the wavelet bases ψ_λ by computing $K\psi_\lambda$ and $K^{\star-1}\psi_\lambda$, where $K^{\star-1}$ denotes the adjoint inverse operator (Tchamitchian 1987). Note that vaguelettes inherit the localization features of wavelets
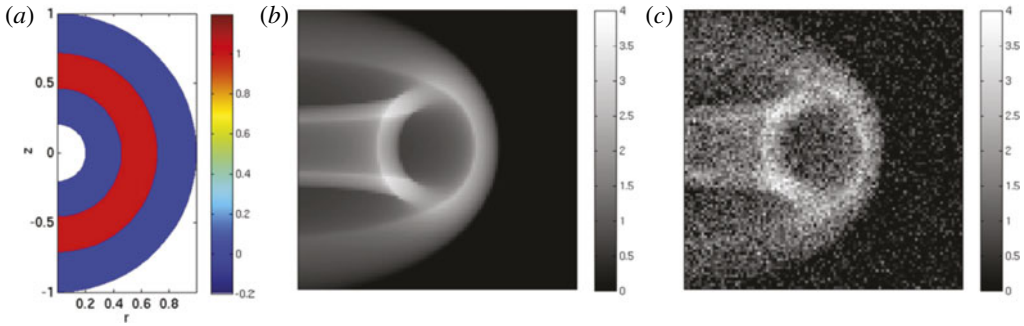
FIGURE 16. Denoising WVD academic test case with a uniform radiating shell. (*a*) Source emission intensity S in the poloidal plane. (*b*) Corresponding noiseless image $I = KS$ in the image plane. (*c*) Noisy image obtained by adding Gaussian white noise with variance 0.5 (from Nguyen van yen *et al.* 2012).
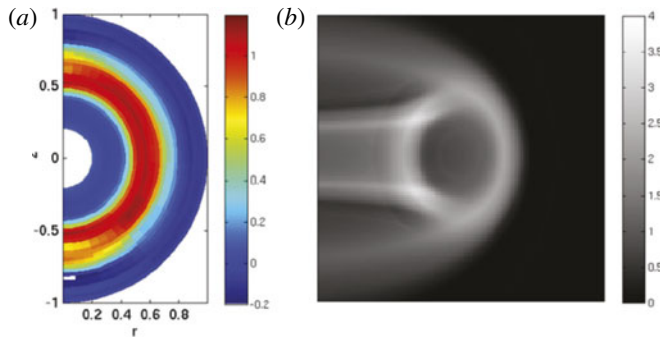

FIGURE 17. Denoising WVD academic test case. WVD inversion results. (*a*) Reconstructed poloidal emissivity map S_d. (*b*) Denoised image $I_d = KS_d$ (from Nguyen van yen *et al.* 2012).

but may lose the translation and scale invariance, and thus the FWT cannot be applied anymore.

3.3.2. *Application to an academic example*

To illustrate the method, we first consider an academic test case with an given emissivity map S, having a uniform radiating shell at constant value one and zero elsewhere. A two-dimensional cut in the poloidal plane is shown in figure 16(*a*). Applying the helical Abel transform we generate the corresponding synthetic image $I = KS$ (figure 16*b*). Then we add a Gaussian white noise with standard deviation 0.5, which yields the synthetic noisy image (figure 16*c*).

Applying the WVD reconstruction to the synthetic noisy image (figure 16*c*) gives a denoised emissivity map, a poloidal cut is shown in figure 17(*a*). We observe that the main features are preserved, i.e. the constant emissivity shell is well recovered, besides some spurious oscillations close to discontinuities. The corresponding denoised image $I_d = KS_d$ (figure 17*b*) illustrates that the noise has been successfully removed. A comparison with the standard SVD technique in Nguyen van yen *et al.* (2012) (not shown here) illustrates the superiority of the wavelet-vaguelette technique.
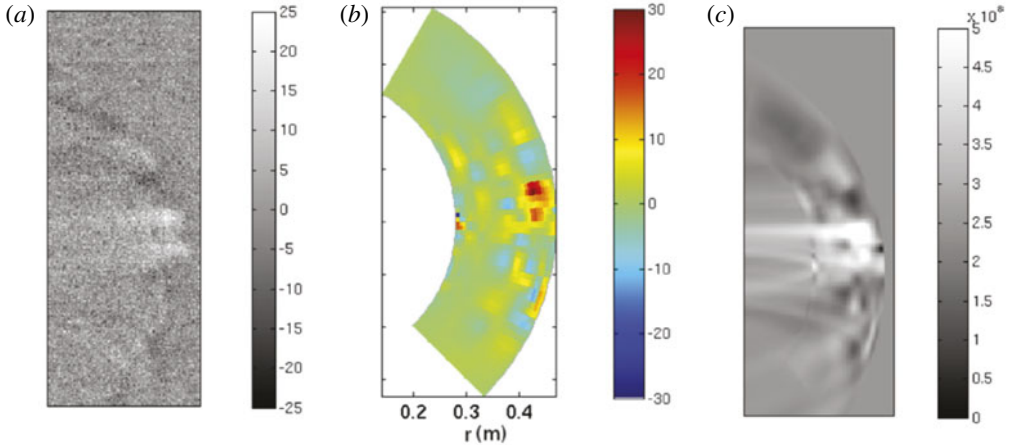
FIGURE 18. WVD-inversion of a snapshot from a movie obtained from Tore Supra, discharge TS42967. (*a*) Noisy frame used as input for the WVD algorithm. (*b*) Reconstructed emissivity map obtained as a result of WVD. (*c*) Denoised frame obtained by applying the operator K to the reconstructed emissivity map (from Nguyen van yen *et al.* 2012).

3.3.3. *Application to fast camera data from tokamaks*

Now we present an application to an experimental movie acquired during the Tore Supra discharge TS42967, where the plasma was fully detached and stabilized over several seconds using a feedback control. The movie has been obtained using a fast camera recording at 40 kHz. Moreover, the time average of the whole movie was subtracted from each frame, which helps us to decrease the effect of reflection on the chamber wall. The algorithm is then applied directly to the fluctuations in the signal instead of the full signal. The experimental conditions can be found in Nguyen van yen *et al.* (2012). One frame of the movie is shown in figure 18(*a*) and used as input for the WVD reconstruction algorithm. The resulting emissivity map in the poloidal plane, in figure 18(*b*), shows the presence of localized blobs, which propagate counter-clockwise, as observed in the movies, not shown here. Thus their propagation velocity can be determined. The corresponding denoised movie frame I_d (figure 18*c*) is obtained by applying the operator K to the inverted emissivity map S_d. We observe that the noise has been removed and the local features such as blobs and fronts have been extracted.

3.4. *Application to two-dimensional simulations of resistive drift-wave turbulence*

At the edge of the plasma in tokamaks drift-waves play an important role in dynamics and transport. In Bos *et al.* (2008) we considered a two-dimensional slab geometry and performed DNS using a two-field model, the Hasegawa–Wakatani system, which describes the main features of resistive drift-waves. The evolution equations for the plasma density fluctuations and the electrostatic potential fluctuations are coupled via the adiabaticity parameter which models the intensity of the parallel electron resistivity. A Poisson equation relates the vorticity with the electrostatic potential. The wavelet-based coherent vortex extraction method (see § 3.1.3) is then applied in Bos *et al.* (2008) to assess the role of coherent vorticity for radial transport and to identify only the active degrees of freedom which are responsible for the transport.
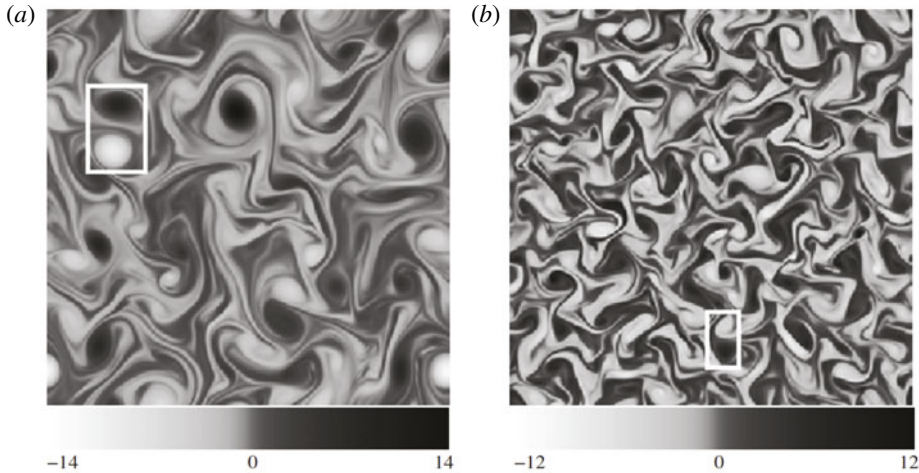
FIGURE 19. Snapshots of the vorticity field for the quasi-hydrodynamic case (*a*) and for the quasi-adiabatic case (*b*). Abscissa and ordinate correspond to the radial and poloidal position, respectively. The white rectangles indicate the selected dipoles (from Bos *et al.* 2008).

Visualizations of the vorticity field for two regimes, the quasi-hydrodynamic case and the quasi-adiabatic case, corresponding, respectively, to low and high collisionality of the plasma, are given in figure 19. In both cases, coherent vortices can be observed and a dipolar structure is framed by the white rectangles. Applying the coherent vorticity extraction (CVE) algorithm, we split the vorticity fields into coherent and incoherent contributions. In the quasi-hydrodynamics case we find that 1.3 % of the wavelet coefficients are sufficient to retain 99.9 % of the energy, while in the quasi-adiabatic case 1.8 % of the modes retain 99 % of the energy. The statistical properties of the total, coherent and incoherent vorticity fields are assessed in figure 20 by plotting the vorticity PDFs and the Fourier enstrophy spectra for the two cases. For the quasi-hydrodynamic vorticity the PDFs of the total and the coherent field are slightly skewed and exhibit a non-Gaussian distribution, while for the quasi-adiabatic case, a symmetric almost Gaussian like distribution can be observed. The variances of the incoherent parts are strongly reduced in both cases with respect to the total fields and the PDFs have a Gaussian-like shape. The enstrophy spectra illustrate that coherent and incoherent contributions exhibit a multiscale behaviour. The spectra of total and coherent vorticity agree well all over the inertial range. The spectra of the incoherent contributions have a powerlaw behaviour close to k^3 which corresponds to an equipartition of kinetic energy. In Bos *et al.* (2008) it is furthermore shown that the radial density flux, i.e. more than 98 %, is indeed carried by these coherent modes. In the quasi-hydrodynamic regime, coherent vortices exhibit depletion of the polarization-drift nonlinearity as shown in the scatter plot of vorticity against the electrostatic potential in figure 21. Moreover, vorticity strongly dominates over strain, in contrast to the quasi-adiabatic regime. Details can be found in Bos *et al.* (2008).

3.5. *Application to three-dimensional simulations of resistive MHD turbulence*

In Yoshimatsu *et al.* (2009*b*) we proposed a method for extracting coherent vorticity sheets and current sheets out of three-dimensional homogeneous MHD turbulence.
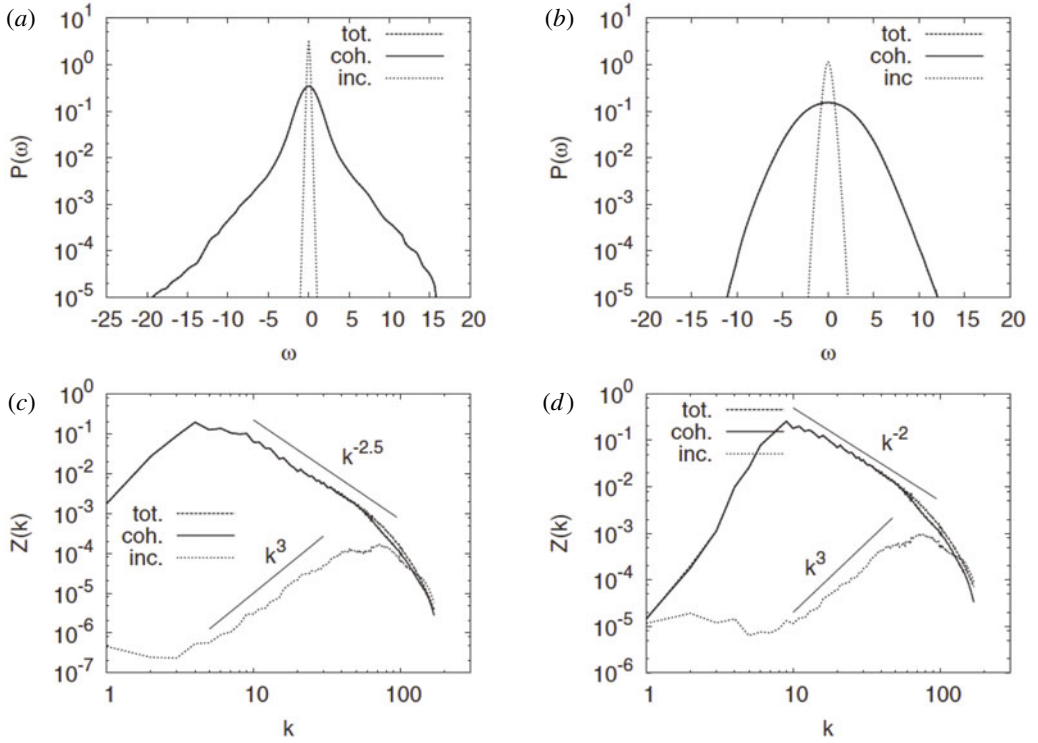
FIGURE 20. (*a*,*b*) PDFs of the vorticity. (*c*,*d*) Fourier spectrum of the enstrophy versus wavenumber. (*a*,*c*) Quasi-hydrodynamic case. (*b*,*d*) Quasi-adiabatic case. Dashed line: total field, solid line: coherent part, dotted line: incoherent part. Note that the coherent contribution (solid) superposes the total field (dashed), which is thus hidden under the solid line in all four figures. The straight lines indicating power laws are plotted for reference (from Bos *et al.* 2008).

To this end the wavelet-based coherent vortex extraction method (see § 3.1.3) has been applied to vorticity and current density fields computed by direct numerical simulation (DNS) of forced incompressible MHD turbulence without mean magnetic field at resolution of 512^3. Coherent vorticity sheets and current sheets are extracted from the DNS data at a given time instant. A visualization of isosurfaces of vorticity and current density of the total, coherent and incoherent fields is shown in figure 22. The coherent vorticity and current density are found to preserve both the vorticity sheets and the current sheets present in the total fields while retaining only a few percent of the degrees of freedom. The incoherent vorticity and current density are shown to be structureless and of mainly dissipative nature. The spectral distributions in figure 23 of kinetic and magnetic energies of the coherent fields only differ in the dissipative range, while the corresponding incoherent fields exhibit quasi-equipartition of energy, corresponding to a k^2 slope. The PDFs of total and coherent fields, for both vorticity and current density in figure 24 coincide almost perfectly, while the incoherent vorticity and current density fields have strongly reduced variances. The energy flux shown in figure 25 confirms that the nonlinear dynamics is indeed fully captured by the coherent fields only. The scale-dependent flatness of the velocity and the magnetic field in figure 26 illustrate that the total and coherent fields have similar scale-dependent high-order moments and reflect strong intermittency characterized
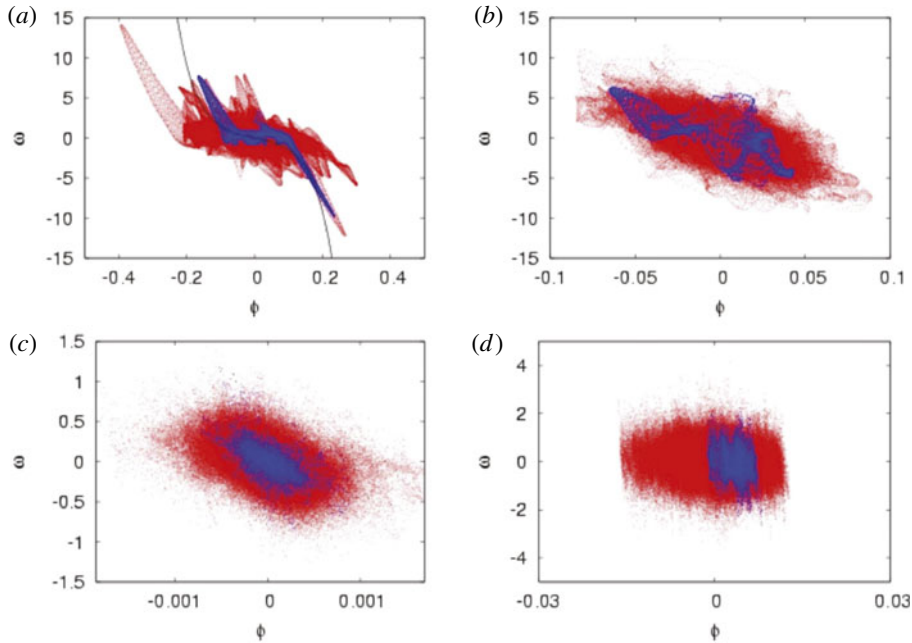
FIGURE 21. Scatter plot of vorticity against electrostatic potential for the coherent part (*a*,*b*) and incoherent part (*c*,*d*). (*a*,*c*) Quasi-hydrodynamic case; (*b*,*d*) quasi-adiabatic case. The red dots correspond to the total field, the blue dots correspond to a selected vortex dipole in figure 19 (from Bos *et al.* 2008).

by the strong increase of the flatness for decreasing scale. The flatness values of the incoherent contributions, of both the velocity and the magnetic field are are much smaller and do not increase significantly for decreasing scale, i.e. they are not intermittent.

4. Wavelet-based simulation schemes

In the following, two wavelet-based methods for solving kinetic plasma equations are presented: an application of nonlinear wavelet denoising to improve the convergence of particle-in-cell (PIC) schemes, and a particle-in-wavelet (PIW) scheme for solving the Vlasov–Poisson equation directly in wavelet space. We also present the coherent vorticity and current sheet simulation (CVCS) method, which extends the coherent vorticity simulation (CVS) method (Farge *et al.* 1999; Farge & Schneider 2001) developed for the Navier–Stokes equations to the resistive non-ideal MHD equations. Numerical examples illustrate the properties and the efficiency of the different methods.

4.1. *Improving particle-in-cell schemes by wavelet denoising*

Plasma simulations using particles are characterized by the presence of noise, a typical feature of Monte-Carlo type simulations. The number of particles, which is restricted by computational resources, limits the statistical sampling and thus the accuracy of the reconstructed particle distribution function.

The discretization error, generically known as particle noise, due to the random-like character of the method quantifies the difference between the distribution function
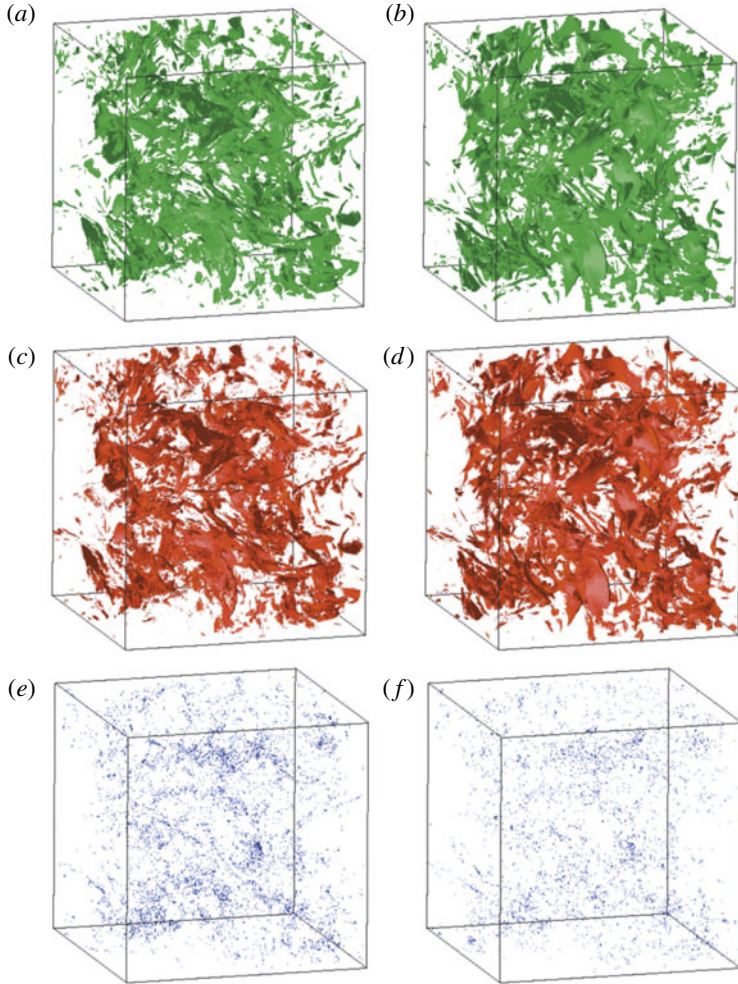
FIGURE 22. Isosurfaces of vorticity (*a,c,e*) and current density (*b,d,f*) of the total (*a,b*), coherent (*c,d*) and incoherent contributions (*e,f*) (from Yoshimatsu *et al.* 2009*b*).

reconstructed from a simulation using N_p particles, and the exact distribution function. The weak scaling of the error with the number of particles, $\propto 1/\sqrt{N_p}$, however, limits the reduction of particle noise by increasing the number of computational particles in practical applications. This has motivated the development of various noise reduction techniques, see, e.g. Nguyen van yen *et al.* (2010), which is of importance in the validation and verification of particle codes.

In Nguyen van yen *et al.* (2010) we proposed a wavelet-based method for noise reduction in the reconstruction of particle distribution functions from particle simulation data, called WBDE. The method was originally introduced in Donoho *et al.* (1996) in the context of statistics to estimate probability densities given a finite number of independent measurements. WBDE, as used in Nguyen van yen *et al.* (2010), is based on a truncation of the wavelet representation of the Dirac delta function associated with each particle. The method yields almost optimal results for functions with unknown local smoothness without compromising computational
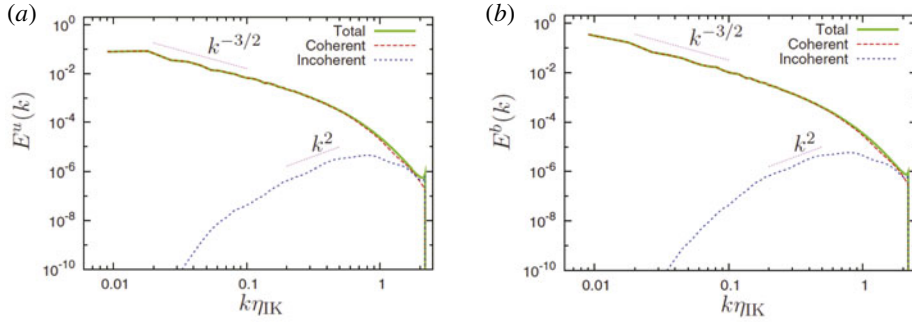
FIGURE 23. Kinetic (*a*) and magnetic (*b*) energy spectra of the total, coherent and incoherent fields. The wavenumber is normalized with the Iroshnikov–Kraichnan scale (from Yoshimatsu *et al.* 2009*b*).
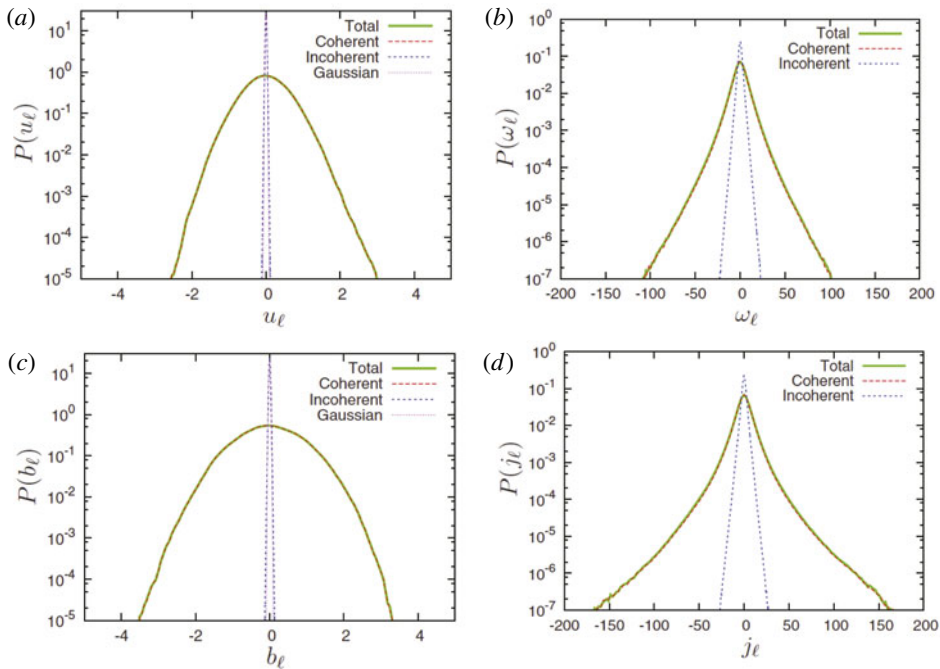

FIGURE 24. PDFs of the ℓth component of the velocity (*a*), vorticity (*b*), magnetic field (*c*) and current density (*d*) for the total, coherent and incoherent contributions (from Yoshimatsu *et al.* 2009*b*).

efficiency, assuming that the particles coordinates are statistically independent. It can be viewed as a natural extension of the finite size particles (FSP) approach, with the advantage of estimating more accurately distribution functions that have localized sharp features. The proposed method preserves the moments of the particle distribution function to a good level of accuracy, has no constraints on the dimensionality of the system, does not require an *a priori* selection of a global smoothing scale, and is able to adapt locally to the smoothness of the density based on the given discrete particle
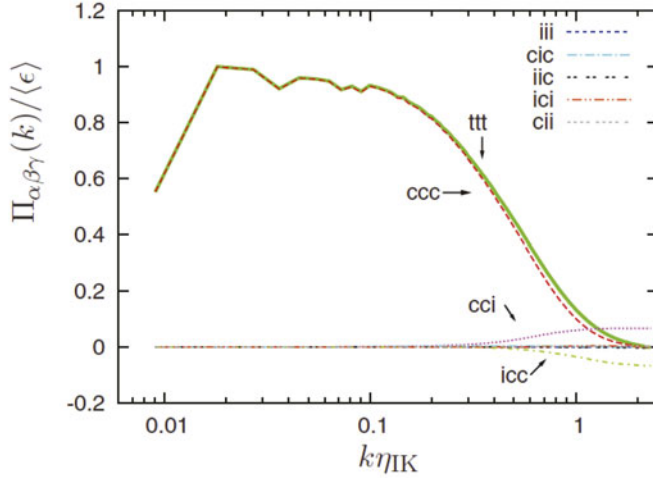
FIGURE 25. Contributions to the energy flux normalized by the energy dissipation rate versus the wavenumber, which is normalized with the Iroshnikov–Kraichnan scale (from Yoshimatsu *et al.* 2009*b*).
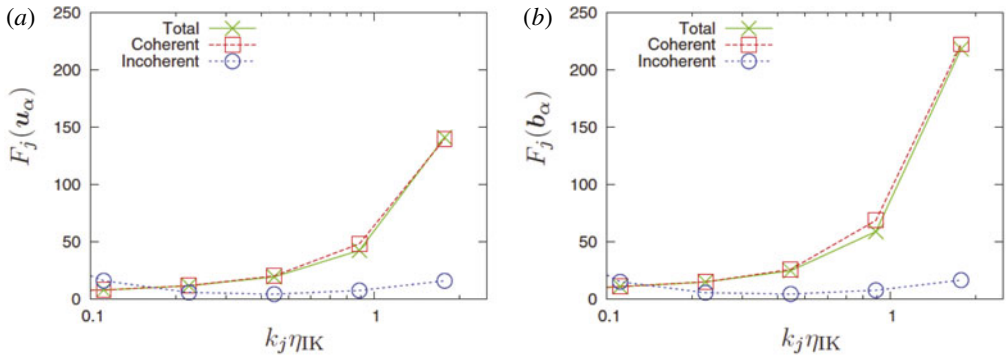

FIGURE 26. Scale-dependent flatness of velocity (*a*) and magnetic field (*b*) versus the wavenumber, which is normalized with the Iroshnikov–Kraichnan scale (from Yoshimatsu *et al.* 2009*b*).

data. Indeed, the projection space is determined from the data itself, which allows for a refined representation around sharp features, and could make the method more precise than PIC for a given computational cost. Moreover, the computational cost of the denoising stage is of the same order as one time step of a FSP simulation.

The underlying idea of WBDE is to expand the sampled particle distribution function, represented by a histogram, into an orthogonal wavelet basis using the FWT. We define the empirical density associated to the particles positions x_n for $n = 1, \ldots, N_p$ where N_p is the number of particles,

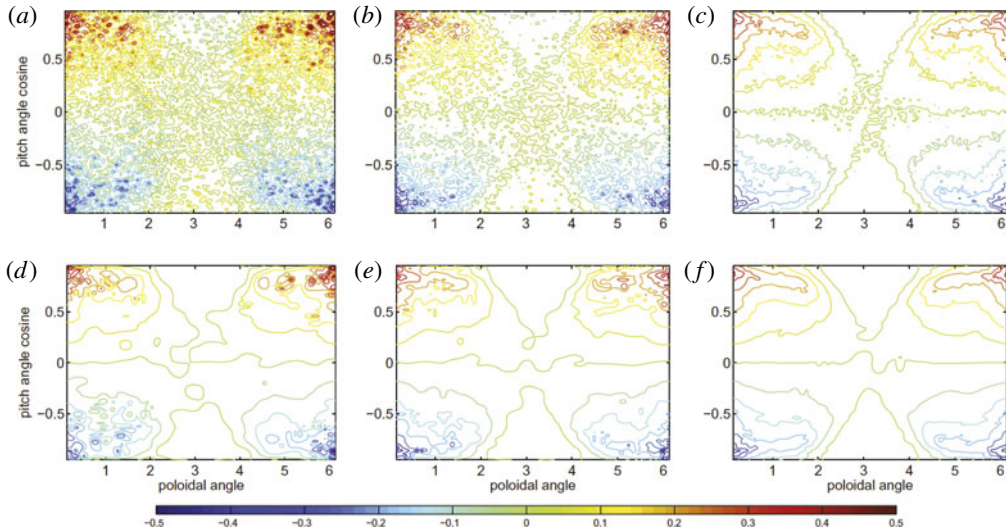$$\rho^{\delta}(x) = \frac{1}{N_p} \sum_{n=1}^{N_p} \delta(x - x_n) \tag{4.1}$$

FIGURE 27. Contour plots of estimates of δf for the collisional guiding centre transport particle data: histogram method (*a–c*) and WBDE method (*d–f*). The (*a–f*) correspond to $N_p = 32 \times 10^3$ (*a,d*), $N_p = 128 \times 10^3$ (*b,e*) and $N_p = 1024 \times 10^3$ (*c,f*), respectively. The plots show 17 isolines equally spaced within the interval [0.5, 0.5] (from Nguyen van yen *et al.* 2010).

and where δ is the Dirac measure. We then project $\rho^\delta(x)$ onto an orthogonal wavelet basis retaining only scales j such that $L \leqslant j \leqslant J$ where the scales L and J denote the largest and smallest retained scales, respectively (Donoho *et al.* 1996). The remaining wavelet coefficients are then thresholded retaining only those whose modulus is larger than the scale-dependent threshold $K\sqrt{j/N_p}$, where K is a constant which depends on the regularity of the solution (Donoho *et al.* 1996). Finally the denoised particle density is obtained by applying an inverse FWT. In Nguyen van yen *et al.* (2010) Daubechies wavelets with six vanishing moments were used.

In Nguyen van yen *et al.* (2010) we treated three cases in order to test how the efficiency of the denoising algorithm depends on the level of collisionality of the plasma. Strongly collisional, weakly collisional and collisionless regimes were considered. For the strongly collisional regime, we computed particle data of force-free collisional relaxation involving energy and pinch-angle scattering. The collisionless regime was studied using PIC-data corresponding to bump-on-tail and two-stream instabilities in the Vlasov–Poisson system. The third case of a weakly collisional regime was illustrated here using guiding-centre particle data of a magnetically confined plasma in toroidal geometry. The data was generated with the code DELTA5D. Figure 27 shows contour plots of the histogram (*a–c*) and the reconstructed densities using WBDE for increasing number of particles. It can be seen that the WBDE results in efficiently denoised densities and that the error has been reduced by a factor two with respect to the raw histograms as shown in figure 28.

4.2. *The particle-in-wavelet scheme*

In Nguyen van yen *et al.* (2011) we proposed a new numerical scheme, called particle-in-wavelet (PIW), for the Vlasov–Poisson equations describing the evolution of the
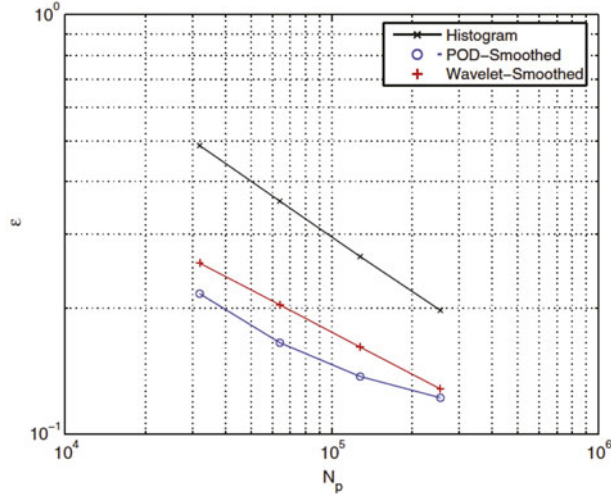
FIGURE 28. R.m.s. error estimate for collisional guiding-centre transport particle data according to the histogram, the proper orthogonal decomposition (POD), and the wavelet methods. The reference density is computed with $N_p = 1024 \times 10^3$ (from Nguyen van yen *et al.* 2010).

particle distribution function f in collisionless plasma, and assessed its efficiency in the simplest case of one spatial dimension. In non-dimensional form, the equations read

$$\partial_t f + v \partial_x f + \partial_x \phi \partial_v f = 0 \qquad (4.2)$$

$$\partial_{xx} \phi + 1 - 2\pi \int_{\mathbb{R}} f(x, v, t) \, \mathrm{d}v = 0, \qquad (4.3)$$

where ϕ is electric potential. The particle distribution function f is discretized using tracer particles, and the charge distribution is reconstructed using WBDE, discussed in the previous section. The latter consists in projecting the Delta distributions corresponding to the particles onto a finite dimensional linear space spanned by a family of wavelets, which are chosen adaptively. A wavelet-Galerkin Poisson solver is used to compute the electric potential once the wavelet coefficients of the electron density $\rho(x, t) = \int_{\mathbb{R}} f(x, v, t) \, \mathrm{d}v$ have been obtained by WBDE. The properties of wavelets are exploited for diagonal preconditioning of the linear system in wavelet space, which is solved by an iterative method, here conjugated gradients. Similar to classical PIC codes, the interpolation method is compatible with the charge assignment scheme. Once the electric field $E(x, t) = -\partial_x \phi(x, t)$ has been interpolated at the particle positions, the characteristic trajectories, defined by $x'(t) = v(t)$ and $v'(t) = -E(x(t), v(t), t)$ can be advanced in time using the Verlet integrator.

To demonstrate the validity of the PIW scheme, numerical computations of Landau damping and of the two-stream instability have been performed in Nguyen van yen *et al.* (2011). The stability and accuracy have been assessed with respect to reference computations obtained with a precise semi-Lagrangian scheme (Sonnendrücker *et al.* 1999). We showed that the precision is improved roughly by a factor three compared to a classical PIC scheme, for a given number of particles (Nguyen van yen *et al.* 2011), as illustrated in figure 29 for the two-stream instability. We observe that PIW
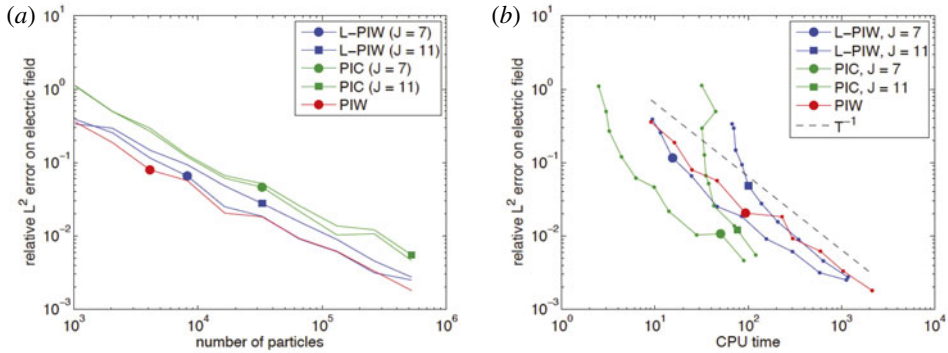
FIGURE 29. Comparisons between PIW and PIC for the two stream instability test case. Relative L^2 error of the electric field at $t = 30$, as a function of the number of particles (*a*) and the corresponding computing time (*b*). Note that L-PIW (linear PIW) is a variant of PIW where only linear filtering has been applied (from Nguyen van yen *et al.* 2011).
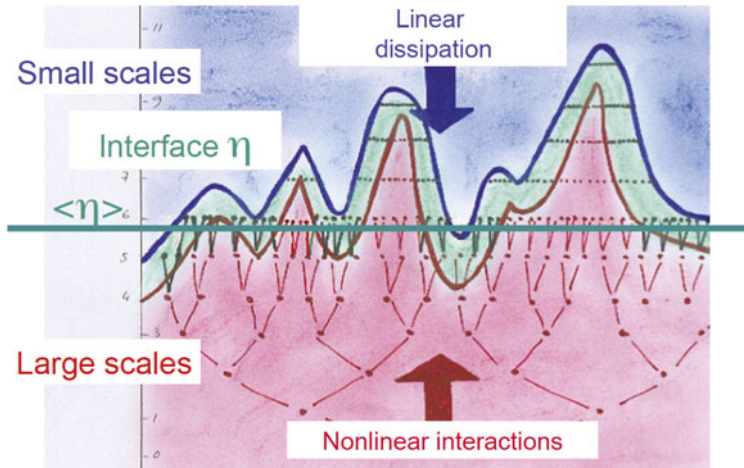

FIGURE 30. Illustration of the safety zone in wavelet coefficient space used in CVS. The degrees of freedom retained by CVE are drawn in red, the adjacent coefficients of the safety zone are drawn in green, while the coefficients in blue correspond to the inactive degrees of freedom which are not computed. The interface η, defined in space and scale, separates the region dominated by nonlinear interaction (red) from the region dominated by linear dissipation (blue). The horizontal green line corresponds to the Kolmogorov dissipation scale $\langle \eta \rangle$ is defined by the statistical mean (either ensemble or space average).

remains consistently more precise for any number of particles thanks to its adaptive properties (figure 29*a*). The total CPU time measured in seconds scaled for the PIW code inversely proportional to the number of particles, while for PIC and L-PIW the scaling changes when the number of particles is too low for a given spatial resolution. However, note that the actual CPU time may depend on the implementation, since the PIC code is written in Fortran while the PIW code is written in C++, although the same computer was used for both codes.
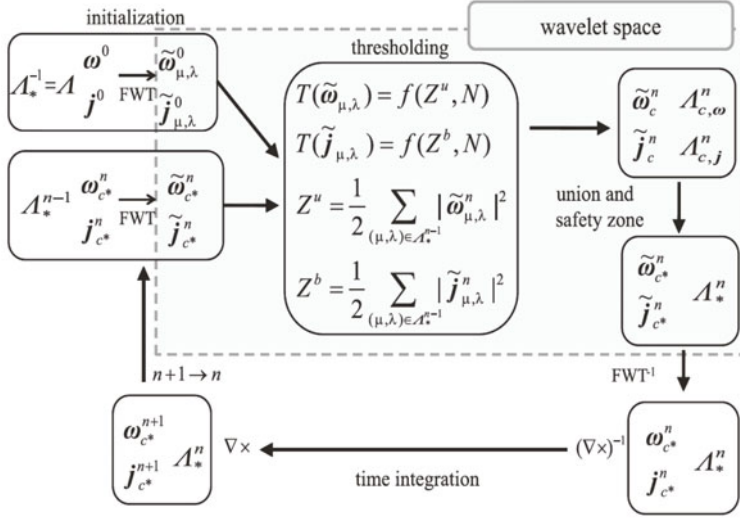
FIGURE 31. Flowchart describing the principle of CVCS. The superscripts n and $n+1$ denote time steps. FWT and FWT^{-1} denote the fast wavelet transform and its inverse. Operators performed in wavelet coefficient space are framed by the dashed rectangle (from Yoshimatsu *et al.* 2013).

4.3. *Coherent vorticity and current sheet simulation*

DNS of turbulent flow has a large computational cost due to the huge number of degrees of freedom to be taken into account. The required spatial resolution thus becomes prohibitive, e.g. scaling as $Re^{9/4}$ for hydrodynamics using Kolmogorov like arguments (Pope 2000). The coherent vorticity simulation (CVS) method, introduced in Farge *et al.* (1999) and Farge & Schneider (2001), proposes to reduce the computational cost by taking only into account the degrees of freedom that are nonlinearly active. To this end, the coherent structure extraction method (presented in § 3) is combined with a deterministic integration of the Navier–Stokes equations. At each time step the CVE is applied to retain only the coherent degrees of freedom, typically a few percent of the coefficients. Then, a set of neighbour coefficients in space and scale, called 'safety zone', is added to account for the advection of coherent vortices and the generation of small scales due to their interaction. Afterwards, the Navier–Stokes equations are advanced in time using this reduced set of a degrees of freedom. Subsequently, the CVE is applied to reduce the number of degrees of freedom and the procedure is repeated for the next time step. A graphical illustration, in wavelet coefficient space of the degrees of freedom retained at a given time step is given in figure 30. This procedure allows us to track the flow evolution in space and scale selecting a reduced number of degrees of freedom in a dynamically adaptive way. With respect to simulations on a regular grid, much less grid points are used in CVS.

In Yoshimatsu *et al.* (2013) we extended CVS to compute three-dimensional incompressible MHD turbulent flow and developed a simulation method called coherent vorticity and current sheet simulation (CVCS). The idea is to track the time evolution of both coherent vorticity and coherent current density, i.e. current sheets. Both the vorticity and current density fields are, respectively, decomposed at each time step into two orthogonal components, corresponding to the coherent
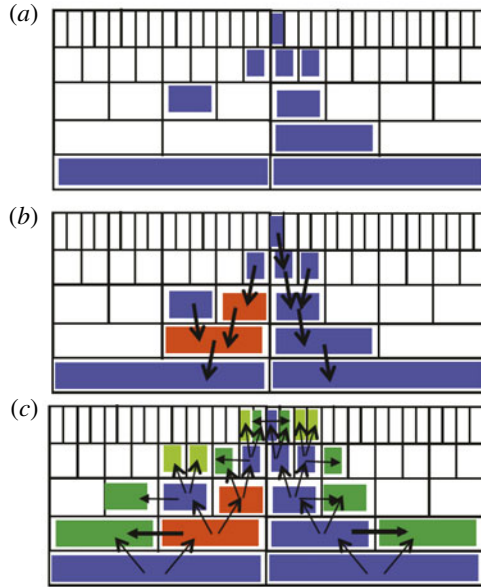
FIGURE 32. Adaption strategy in wavelet coefficient space used in CVCS: (*a*) retained wavelet coefficients (blue), (*b*) added wavelet coefficients to ensure a graded tree (red) and (*c*) added wavelet coefficients corresponding to the safety zone (green).

and incoherent contribution, using an orthogonal wavelet representation. Each of the coherent fields is reconstructed from the wavelet coefficients whose modulus is larger than a threshold, while their incoherent counterparts are obtained from the remaining coefficients. The two threshold values depend on the instantaneous kinetic and magnetic enstrophies. The induced coherent velocity and magnetic fields are computed from the coherent vorticity and current density, respectively, using the Biot–Savart kernel. In order to compute the flow evolution, one should retain not only the coherent wavelet coefficients but also their neighbours in wavelet space, the safety zone. A flowchart summarizing the principle of CVCS is shown in figure 31 and the adaption strategy in orthogonal wavelet coefficient space in figure 32.

In Yoshimatsu *et al.* (2013) CVCS was performed for three-dimensional forced incompressible homogeneous MHD turbulence without a mean magnetic field, for a magnetic Prandtl number equal to unity. The Navier–Stokes equations coupled with the induction equation were solved with a pseudospectral method using 256^3 grid points and integrated in time with a Runge–Kutta scheme. Different adaption strategies to select the optimal saftey zone for CVCS have been studied. We tested the influence of the safety zone and of the threshold, as defined in § 3.1.3, by considering three cases:

 (i) CVCS0 with safety zone but without iterating the threshold ϵ_0;
 (ii) CVCS1 with safety zone but with iterating the threshold once ϵ_1;
(iii) CVCS2 without safety zone but without iterating the threshold ϵ_0;

details can be found in Yoshimatsu *et al.* (2013). The quality of CVCS was then assessed by comparing the results with a DNS. It is found that CVCS with the safety zone well preserves the statistical predictability of the turbulent flow with a reduced number of degrees of freedom. CVCS was also compared with a Fourier truncated
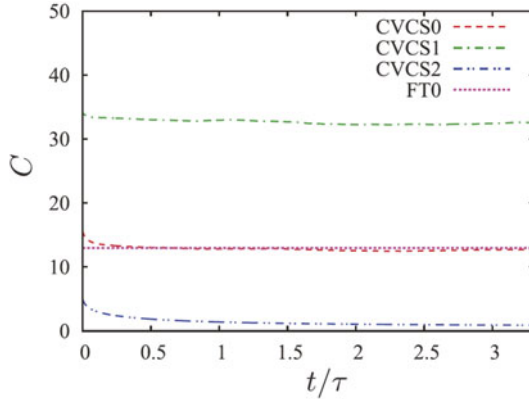
FIGURE 33. Evolution of the percentage C of retained wavelet coefficients for CVCS with three different adaption strategies in comparison with Fourier filtering (FT0) with a fixed cutoff wavenumber (from Yoshimatsu *et al.* 2013).

simulation using a spectral cutoff filter, where the number of retained Fourier modes is similar to the number of the wavelet coefficients retained by CVCS0. Figure 33 shows the percentage of retained wavelet coefficients for CVCS (with three different adaption strategies) in comparison to Fourier filtering (FT0) with a fixed cutoff wavenumber. The percentage of retained kinetic energy, magnetic energy, kinetic enstrophy and magnetic enstrophy for the three different CVCS strategies in comparison with Fourier filtering (FT0) is plotted in figure 34.

Probability density functions of vorticity and current density, normalized by the corresponding standard deviation, in figure 35 show that CVCS0 and CVCS1 capture well the high-order statistics of the flow, while in FT0 and in CVCS2 the tails of the PDFs are reduced with respect to the DNS results. The energy spectra of kinetic and magnetic energy in figure 36 confirm that CVCS0 and CVCS1 reproduce perfectly the DNS results in the inertial range, where all nonlinear acticity takes place, and only differs in the dissipative range.

The results thus show that the wavelet representation is more suitable than the Fourier representation, especially concerning the probability density functions of vorticity and current density and that only about 13 % of the degrees of freedom (CVCS0) compared to DNS are sufficient to represent the nonlinear dynamics of the flow. A visualization comparing both the vorticity and current density field for DNS and CVCS0 is presented in figure 37.

5. Conclusion

This paper reviewed different wavelet techniques and showed several of their applications to MHD and plasma turbulence. Continuous and orthogonal wavelet transforms were presented and some wavelet-based statistical tools described, after selecting those most appropriate to study turbulence, such as scale-dependent second- and higher-order moments, intermittency measure, together with scale-dependent directional statistical measures. Examples of applications to three-dimensional incompressible MHD turbulence, computed by DNS, illustrated how the flow intermittency can be quantified and how its anisotropy and helicity might vary with scale. The wavelet-based coherent structure extraction algorithm was detailed
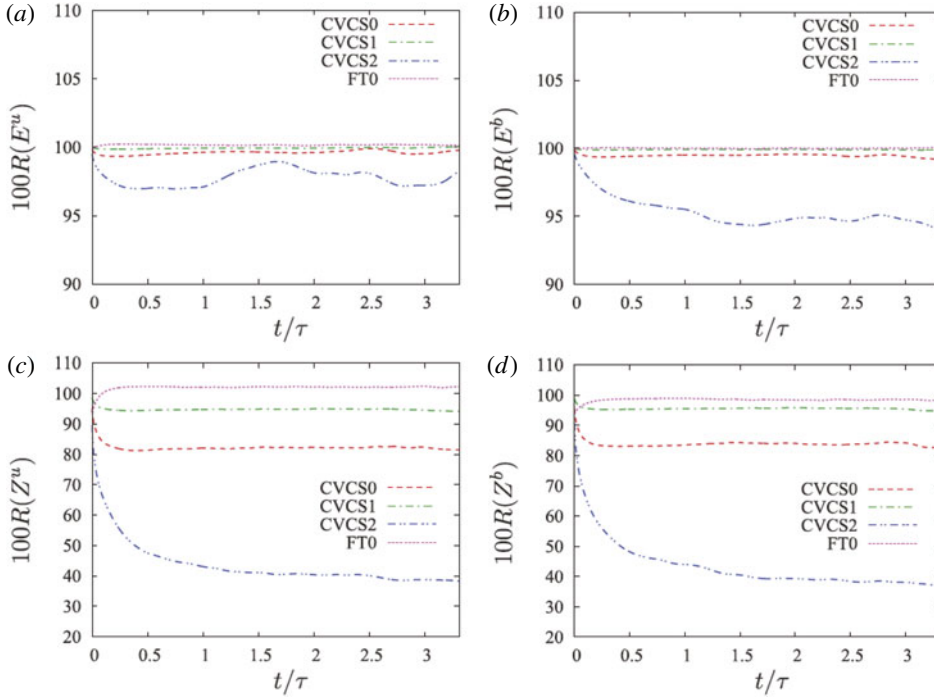
FIGURE 34. Percentage of retained kinetic energy (*a*), magnetic energy (*b*), kinetic enstrophy (*c*) and magnetic enstrophy (*d*) for the three different CVCS strategies in comparison with Fourier filtering (FT0) (from Yoshimatsu *et al.* 2013).
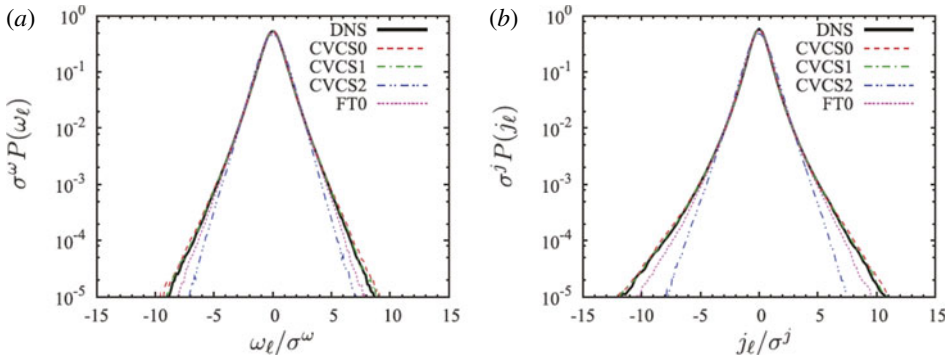

FIGURE 35. PDFs of the ℓth component of vorticity (*a*) and current density (*b*) normalized by the corresponding standard deviation (from Yoshimatsu *et al.* 2013).

and validated for a test signal. Different applications to experimental and numerical turbulent plasma data, in one, two and three dimensions, were shown. The underlying methodology of a wavelet-based tomographic reconstruction algorithm for denoising images and movies obtained with fast cameras in tokamaks were explained and results were presented. Applications to an academic example and to fast camera data from Tore Supra proved the efficiency of the algorithm to extract blobs and fronts while denoising the data. Wavelet-based simulation schemes developed in the context
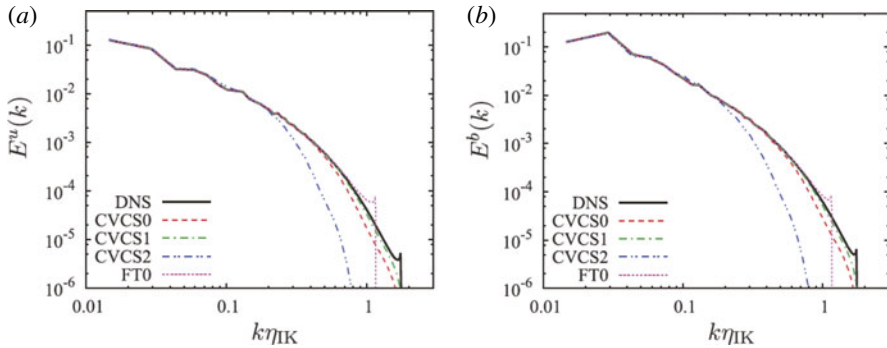
FIGURE 36. Kinetic (*a*) and magnetic energy spectra (*b*). The wavenumber is normalized with the Iroshnikov–Kraichnan scale (from Yoshimatsu *et al.* 2013).
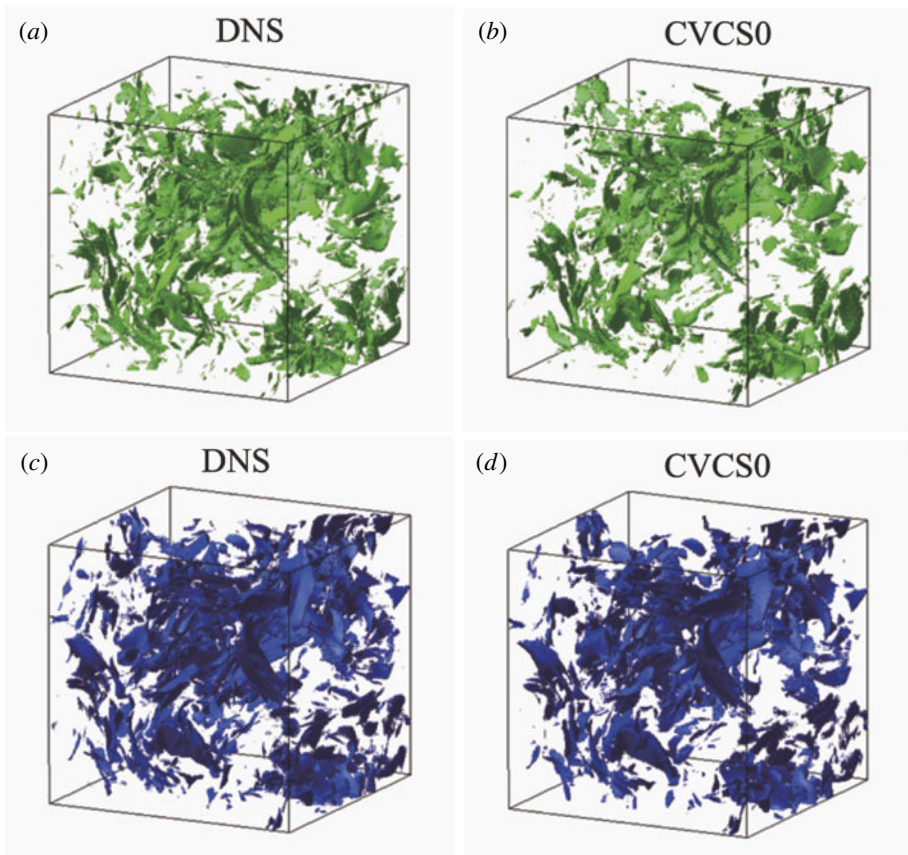

FIGURE 37. Visualization of isosurfaces of modulus of vorticity (*a,b*) and modulus of current density (*c,d*) for DNS (*a,c*) and CVCS0 (*b,d*) (from Yoshimatsu *et al.* 2013).

of kinetic plasma equations were also described. Results computed with them showed how wavelet denoising accelerates the convergence of classical PIC schemes and how a PIW scheme solves the Vlasov–Poisson equation directly and efficiently in wavelet

space. Concerning the fluid equations, in particular the resistive non-ideal MHD equations, the CVS and CVCS methods were explained and examples illustrated the properties and insights the wavelet-based approach offers in the context of MHD and plasma turbulence.

Acknowledgements

REFERENCES

ADDISON, P. S. 2002 *The Illustrated Wavelet Transform Handbook: Introductory Theory and Applications in Science, Engineering, Medicine and Finance*. Taylor & Francis.

ALEXANDROVA, O., LACOMBE, C. & MANGENEY, A. 2008 Spectra and anisotropy of magnetic fluctuations in the Earth's magnetosheath: cluster observations. *Ann. Geophys.* **26**, 3585–3596.

AZZALINI, A., FARGE, M. & SCHNEIDER, K. 2005 Nonlinear wavelet thresholding: a recursive method to determine the optimal threshold value. *Appl. Comput. Harmon. Anal.* **18** (2), 177–185.

BATCHELOR, G. K. 1982 *The Theory of Homogeneous Turbulence*. Cambridge University Press.

BISKAMP, D. 1997 *Nonlinear Magnetohydrodynamics*. Cambridge University Press.

BOS, W. J. T., FUTATANI, S., BENKADDA, S., FARGE, M. & SCHNEIDER, K. 2008 The role of coherent vorticity for turbulent transport in resistive drift-wave turbulence. *Phys. Plasmas* **15**, 072305.

BOS, W. J. T., LIECHTENSTEIN, L. & SCHNEIDER, K. 2007 Small scale intermittency in anisotropic turbulence. *Phys. Rev.* E **76**, 046310.

CARBONE, V., REGNOLI, G., MARTINES, E. & ANTONI, V. 2000 Intermittency and self-similarity in plasma edge fluctuations. *Phys. Plasmas* **7** (2), 445–447.

DAUBECHIES, I. 1992 *Ten Lectures on Wavelets*. SIAM.

DERIAZ, E., FARGE, M. & SCHNEIDER, K. 2010 Craya decomposition using compactly supported biorthogonal wavelets. *Appl. Comput. Harmon. Anal.* **28**, 267–284.

DONOHO, D. 1995 Nonlinear solution of linear inverse problems by wavelet-vaguelette decomposition. *Appl. Comput. Harmon. Anal.* **2** (2), 101–127.

DONOHO, D. & JOHNSTONE, I. 1994 Ideal spatial adaptation via wavelet shrinkage. *Biometrika* **81**, 425–455.

DONOHO, D., JOHNSTONE, I., KERYACHARIAN, G. & PICARD, D. 1996 Density estimation by wavelet thresholding. *Ann. Stat.* **24** (2), 508–539.

DOSE, V., VENUS, G. & ZOHM, H. 1997 Wavelet analysis of fusion plasma transients. *Phys. Plasmas* **4** (2), 323–328.

DUDOK DE WIT, T., ALEXANDROVA, O., FURNO, I., SORRISO-VALVO, L. & ZIMBARDO, G. 2014 Methods for characterising microphysical processes in plasmas. In *Microphysics of Cosmic Plasmas*, pp. 589–617. Springer.

DUDOK DE WIT, T. & KRASNOSELSKIKH, V. V. 1995 Wavelet bicoherence analysis of strong plasma turbulence at the Earths quasiparallel bow shock. *Phys. Plasmas* **2** (11), 4307–4311.

FARGE, M. 1992 Wavelet transforms and their applications to turbulence. *Annu. Rev. Fluid Mech.* **24**, 395–457.

FARGE, M., PELLEGRINO, G. & SCHNEIDER, K. 2001 Coherent vortex extraction in 3D turbulent flows using orthogonal wavelets. *Phys. Rev. Lett.* **87** (5), 45011–45014.

FARGE, M. & RABREAU, G. 1988 Transformée en ondelettes pour détecter et analyser les structures cohérentes dans les écoulements turbulents bidimensionnels. *C. R. Acad. Sci. Paris* **307**, 1479–1486; série II.

FARGE, M. & SCHNEIDER, K. 2001 Coherent vortex simulation (CVS), a semi-deterministic turbulence model using wavelets. *Flow Turbul. Combust.* **6**, 393–426.

FARGE, M. & SCHNEIDER, K. 2006 Wavelets: applications to turbulence. In *Encyclopedia of Mathematical Physics* (ed. J.-P. Françoise, G. Naber & T. S. Tsun), pp. 408–419. Elsevier.

FARGE, M., SCHNEIDER, K. & DEVYNCK, P. 2006 Extraction of coherent events in turbulent edge plasma using orthogonal wavelets. *Phys. Plasmas* **13**, 042304.

FARGE, M., SCHNEIDER, K. & KEVLAHAN, N. 1999 Non-Gaussianity and coherent vortex simulation for two-dimensional turbulence using adaptive orthonormal wavelet basis. *Phys. Fluids* **11**, 2187–2201.

FARGE, M., SCHNEIDER, K., PELLEGRINO, G., WRAY, A. & ROGALLO, R. 2003 Coherent vortex extraction in three-dimensional homogeneous isotropic turbulence: comparison between CVS and POD decompositions. *Phys. Fluids* **15** (10), 2886–2896.

FRISCH, U. 1995 *Turbulence*. Cambridge University Press.

GROSSMANN, A. & MORLET, J. 1984 Decomposition of Hardy functions into square integrable wavelets of constant shape. *SIAM J. Math. Anal.* **15** (4), 723–736.

KOLMOGOROV, A. N. 1962 A refinement of previous hypotheses concerning the local structure of turbulence in a viscous incompressible fluid at high Reynolds number. *J. Fluid Mech.* **13**, 82–85.

KURIEN, S. & SREENIVASAN, K. R. 2000 Anisotropic scaling contributions to high-order structure functions in high-Reynolds-number turbulence. *Phys. Rev.* E **62** (2), 2206–2212.

KURIEN, S. & SREENIVASAN, K. R. 2001 *New Trends in Turbulence* (ed. M. Lesieur, A. Yaglom & F. David), EDP Sciences.

MALLAT, S. 1998 *A Wavelet Tour of Signal Processing*. Academic Press.

MENEVEAU, C. 1991 Analysis of turbulence in the orthonormal wavelet representation. *J. Fluid Mech.* **232**, 469.

NGUYEN VAN YEN, R., DEL CASTILO-NEGRETE, D., SCHNEIDER, K., FARGE, M. & CHEN, G. Y. 2010 Wavelet–based density estimation for noise reduction in plasma simulation using particles. *J. Comput. Phys.* **229** (8), 2821–2839.

NGUYEN VAN YEN, R., FEDORCZAK, N., BROCHARD, F., BONHOMME, G., SCHNEIDER, K., FARGE, M. & MONIER-GARBET, P. 2012 Tomographic reconstruction of tokamak plasma light emission from single using wavelet-vaguelette decomposition. *Nucl. Fusion* **52**, 013005.

NGUYEN VAN YEN, R., SONNENDRÜCKER, E., SCHNEIDER, K. & FARGE, M. 2011 Particle-in-wavelets scheme for the 1D Vlasov–Poisson equations. *ESAIM: Proc.* **32**, 134–148.

OKAMOTO, N., YOSHIMATSU, K., SCHNEIDER, K. & FARGE, M. 2011 Directional and scale-dependent statistics of quasi-static magnetohydrodynamic turbulence. *ESAIM: Proc.* **32**, 95–102.

OKAMOTO, N., YOSHIMATSU, K., SCHNEIDER, K. & FARGE, M. 2014 Small-scale anisotropic intermittency in magnetohydrodynamic turbulence at low magnetic Reynolds number. *Phys. Rev.* E **89**, 033013.

POPE, S. 2000 *Turbulent Flows*. Cambridge University Press.

SANDBORN, V. A. 1959 Measurements of intermittency of turbulent motion in a boundary layer. *J. Fluid Mech.* **6**, 221–240.

SCHNEIDER, K. & FARGE, M. 2006 Wavelets: mathematical theory. In *Encyclopedia of Mathematical Physics* (ed. J.-P. Françoise, G. Naber & T. S. Tsun), pp. 426–437. Elsevier.

SCHNEIDER, K., FARGE, M. & KEVLAHAN, N. 2004 Spatial intermittency in two-dimensional turbulence: a wavelet approach. In *Woods Hole Mathematics, Perspectives in Mathematics and Physics* (ed. N. Tongring & R. C. Penner), vol. 34, pp. 302–328. World Scientific.

SCHNEIDER, K. & VASILYEV, O. 2010 Wavelet methods in computational fluid dynamics. *Annu. Rev. Fluid Mech.* **42**, 473–503.

SONNENDRÜCKER, E., ROCHE, J., BERTRAND, P. & GHIZZO, A. 1999 The semi-Lagrangian method for the numerical resolution of the Vlasov equation. *J. Comput. Phys.* **149**, 201–220.

SORRISO-VALVO, L., CARBONE, V., BRUNO, R. & VELTRI, P. 2006 Persistence of small-scale anisotropy of magnetic turbulence as observed in the solar wind. *Europhys. Lett.* **75** (5), 832.

TCHAMITCHIAN, P. 1987 Biorthogonalité et théorie des opérateurs. *Rev. Mat. Iberoam.* **3**, 163–189.

VAN MILLIGEN, B. P., HIDALGO, C. & SANCHEZ, E. 1995*b* Nonlinear phenomena and intermittency in plasma turbulence. *Phys. Rev. Lett.* **74** (3), 395.

VAN MILLIGEN, B. P., SANCHEZ, E., ESTRADA, T., HIDALGO, C., BRANAS, B., CARRERAS, B. & GARCIA, L. 1995*a* Wavelet bicoherence: a new turbulence analysis tool. *Phys. Plasmas* **2** (8), 3017–3032.

YOSHIMATSU, K., KONDO, Y., SCHNEIDER, K., OKAMOTO, N., HAGIWARA, H. & FARGE, M. 2009*b* Wavelet based coherent vorticity sheet and current sheet extraction from three-dimensional homogeneous magnetohydrodynamic turbulence. *Phys. Plasmas* **16**, 082306.

YOSHIMATSU, K., OKAMOTO, N., KAWAHARA, Y., SCHNEIDER, K. & FARGE, M. 2013 Coherent vorticity and current density simulation of three-dimensional magnetohydrodynamic turbulence using orthogonal wavelets. *Geophys. Astrophys. Fluid Dyn.* **107** (1–2), 73–92.

YOSHIMATSU, K., OKAMOTO, N., SCHNEIDER, K., KANEDA, Y. & FARGE, M. 2009*a* Intermittency and scale-dependent statistics in fully developed turbulence. *Phys. Rev.* E **79**, 026303.

YOSHIMATSU, K., SCHNEIDER, K., OKAMOTO, N., KAWAHARA, Y. & FARGE, M. 2011 Intermittency and geometrical statistics of three-dimensional homogeneous magnetohydrodynamic turbulence: a wavelet viewpoint. *Phys. Plasmas* **18**, 092304.